Electronic Supplementary Information

Unusual Polar Ordering and Room-Temperature Blue Phase Stabilization in Tetrafluorinated Bent-Shaped Mesogens

Anshika Baghla,†[a] Mudit Sahai,†[b,c] Neelam Yadav,[b] Santosh Prasad Gupta,[d] Vidhika Punjani,[a,e] V. Manjuladevi,[c] Jagdish K. Vij,*[b] Santanu Kumar Pal*[a]

[a]Department of Chemical Sciences, Indian Institute of Science Education and Research (IISER) Mohali, Sector-81, Knowledge City, Manauli-140306, India;
E-mail: skpal@iisermohali.ac.in

[b]Department of Electronic and Electrical Engineering, Trinity College Dublin, The University of Dublin, Dublin 2, Ireland;
E-mail: jvij@tcd.ie

[c]Department of Physics, Birla Institute of Technology and Science, Pilani (BITS Pilani), Rajasthan, 333031, India

[d]Department of Physics, Patna University, Patna-800005, India

[e]Centre of Molecular and Macromolecular Studies, Polish Academy of Sciences, 90-363 Łódź, Poland

†(Joint first authors)

Table of contents

1. Experimental details

Materials: Chemicals and solvents of analytical reagent (AR) grade were used directly without further purification. Column chromatography separations were carried out using silica gel with particle sizes of 100-200 mesh and 60-120 mesh. Thin-layer chromatography (TLC) was performed on aluminum sheets pre-coated with silica gel (Merck Kieselgel 60, F254). Commercially available S811 and 5CB were procured from TCI chemicals.

Instrumentation: The instrumentation details for structural characterization (including NMR, FT-IR, and UV-visible spectroscopy), thermal analysis, polarized optical microscopy (POM), and small-angle/wide-angle X-ray scattering (SAXS/WAXS) have been previously reported.[1] 2D images for SAXS/WAXS measurements were processed using ImageJ software. Differential scanning calorimetry (DSC) was done using a Mettler Toledo DSC 821e. Birefringence measurements were carried out using an Olympus BX 52 Polarizing Optical Microscope, with samples placed in planar (antiparallel buffing) and homeotropic alignment cells obtained from E.H.C. Co. Ltd, Japan, and transmittance measured via an Avantes AvaSpec-2048 fiber spectrometer. Dielectric spectroscopy (DS) measurements were conducted using broadband alpha high-resolution dielectric analyzer (Novocontrol GmbH, Germany). Indium tin oxide (ITO) coated glass substrates with different sheet resistances (~10 Ω/□ and ~200 Ω/□) along with Mylar spacers of 9 μm thickness were used to construct the lab-made LC cells for the dielectric measurements. Planar and homeotropic alignments were achieved by spin-coating ITO glass substrates with RN1175 (Nissan Chemicals, Japan) and polymer solution AL60702 (JSR, Korea), respectively. The temperature of the sample cells was stabilized to within ±0.02 °C using a Eurotherm 2604 temperature controller. DFT calculations were performed using Gaussian 16 and GaussView 5.0.

2. Synthesis and Chemical Characterization

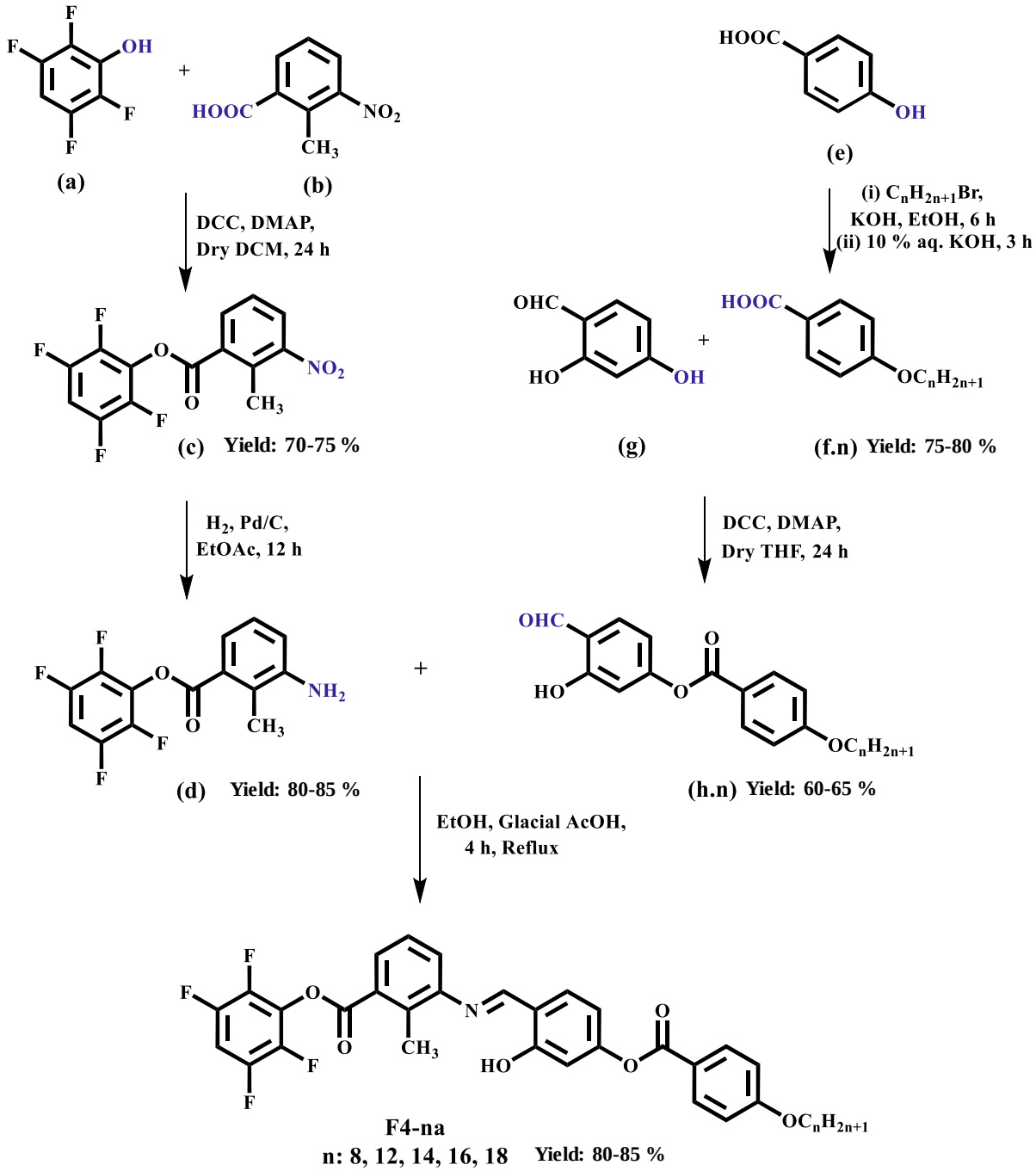

Scheme S1. Synthetic scheme for **F4-na** series of compounds.

Synthesis of compound (c) 2,3,5,6-tetrafluorophenyl 2-methyl-3-nitrobenzoate

The intermediate compound (**c**) was synthesized via Steglich esterification reaction, following a similar procedure previously reported[1] and reproduced below:

2-methyl-3-nitrobenzoic acid (**b**, 1.50 g, 8.3 mmol, 1 equivalent) was dissolved in 20 ml dry dichloromethane (DCM) under a nitrogen atmosphere, with the addition of a catalytic amount of 4-dimethylaminopyridine (DMAP). Subsequently, 2.14 g (10.4 mmol, 1.25 equivalents) of

N,N'-dicyclohexylcarbodiimide (DCC) was added. The reaction mixture was stirred for 30 min, and then 1.51 g (9.1 mmol, 1.1 equivalents) of 2,3,5,6-tetrafluorophenol (**a**) was added. The resulting mixture was allowed to stir at room temperature for 24 h. Following this, the solid by-product formed (dicyclohexylurea, DCU) was removed via filtration, and the residual mixture was concentrated using a rotary evaporator. The purification was done via column chromatography, using silica gel (100-200 mesh) and ethyl acetate-hexane. The white solid product (**c**) was obtained with 70-75 % yield (1.96 g).

^{1}H NMR (400 MHz, $CDCl_3$, δ in ppm) δ = 8.32 - 8.30 (dd, 1H, Ar-H), 8.00 - 7.98 (dd, 1H, Ar-H), 7.55 - 7.51 (t, 1H, Ar-H), 7.14 - 7.05 (m, 1H, Ar-H), 2.72 (s, 3H, -CH_3).

^{13}C {^{1}H} NMR (100 MHz, $CDCl_3$, δ in ppm) δ = 161.82, 152.28, (147.46, 147.38, 147.34, 147.26, C atom bonded to F showing C-F splitting), (145.02, 144.91, 144.86, C atom bonded to F), (142.01, 141.84, 141.83, C atom bonded to F), (139.47, 139.46, 139.34, C atom bonded to F), 134.73, 134.49, 129.99, 129.34 (aromatic C in fluorinated ring), 128.28, 126.94, (104.01, 103.78, 103.56, 103.55, aromatic C in fluorinated ring), (16.23, 16.20, -CH_3 on central core).

Synthesis of compound (d) 2,3,5,6-tetrafluorophenyl 3-amino-2-methylbenzoate

Compound (**d**) was synthesized through the reduction of the nitro group present in compound (**c**) via a hydrogenation reaction. 1.50 g (4.6 mmol) of Compound (**c**) was dissolved in ethyl acetate (10 ml), and 75 mg (5 wt%) of palladium on activated charcoal catalyst was added. The reaction mixture was then stirred under a hydrogen (H_2) atmosphere at room temperature. After 12 h, the catalyst was removed by filtration, and the resulting residue was concentrated via solvent evaporation, yielding product (**d**) as a brownish solid with an 80-85% yield (1.14 g).

^{1}H NMR (400 MHz, $CDCl_3$, δ in ppm) δ = 7.56 - 7.53 (dd, 1H, Ar-H), 7.17 - 7.13 (t, 1H, Ar-H), 7.07 - 6.98 (m, 1H, Ar-H), 6.94 - 6.92 (dd, 1H, Ar-H), 3.84 (br s, 2H, -NH_2), 2.42 (s, 3H, -CH_3).

^{13}C {^{1}H} NMR (100 MHz, $CDCl_3$, δ in ppm) δ = 163.89, (147.47, 147.36, 147.31, 147.19, C atom bonded to F showing C-F splitting), 145.91, 144.89 (C atom bonded to F), (142.20, 142.02, C atom bonded to F), (139.70, 139.58, C atom bonded to F), 130.03 (aromatic C in fluorinated ring), 127.91, 126.44, 124.53, 121.51, 119.87, (103.34, 103.11, 102.88, aromatic C in fluorinated ring), (13.86, 13.83, -CH_3 on central core).

Synthesis of compound (h.n) 4-formyl-3-hydroxyphenyl 4-(n-alkoxy)benzoate

The general procedure for synthesizing intermediate compound **(h.n)** is similar as reported earlier[1] and briefly discussed below:

4-hydroxybenzoic acid (**e**, 1 g, 7.2 mmol, 1 equivalent) was mixed with an ethanolic solution (20 ml) of 2.5 equivalents KOH (1.02 g, 18 mmol) under refluxing conditions. To the mixture, 1.2 equivalent (8.6 mmol) of n-alkyl bromide ($C_nH_{2n+1}Br$) were added (for n : 8, 12, 14, 16, 18) and allowed to reflux for 6 h. Further, 10 % aqueous KOH solution (5-10 ml) was added, and

the mixture was refluxed for 3 h to hydrolyze any formed esters. The reaction mixture was then neutralized by pouring in acid water, resulting in the appearance of a white solid product upon stirring. The product was collected via filtration and washed with water, yielding 75-80% of the desired compounds (**f.n**).

The obtained 4-alkoxybenzoic acid (**f.n**) was then dissolved (1.0 g, 1 equivalent) in 10 ml dry Tetrahydrofuran (THF) under nitrogen atmosphere followed by the addition of a catalytic amount of DMAP. Further, 1.2 equivalents of DCC were added to it followed by the addition of 1 equivalent (with respect to **f.n**) of 2,4-dihydroxybenzaldehyde (**g**). The reaction mixture was stirred for 24 hours at room temperature. The by-product DCU precipitated out and was removed by filtration. The filtrate was concentrated by evaporating the solvent and the crude product was obtained which was purified by column chromatography using silica gel and hexane-ethyl acetate as eluent (60-65 % yield).

The ^{1}H and ^{13}C NMR data for one of the intermediate homologue (representative compound **h.12**) is reported earlier[1].

Synthesis of final compound (F4-na) 2,3,5,6-tetrafluorophenyl (E)-3-((2-hydroxy-4-((4-(alkyloxy)benzoyl)oxy)benzylidene)amino)-2-methylbenzoate

The aldehyde **h.n** (250 mg, 1 equivalent) was dissolved in absolute ethanol (10 ml) containing a few drops of glacial acetic acid. Further, 1 equivalent of amine **d** (with respect to **h.n**) was added to the reaction mixture, which was then refluxed for 4 h. Upon cooling, a yellow solid product was obtained, which was isolated by filtration and washed with ethanol, yielding 80-85% of the final product.

Compound F4-8a

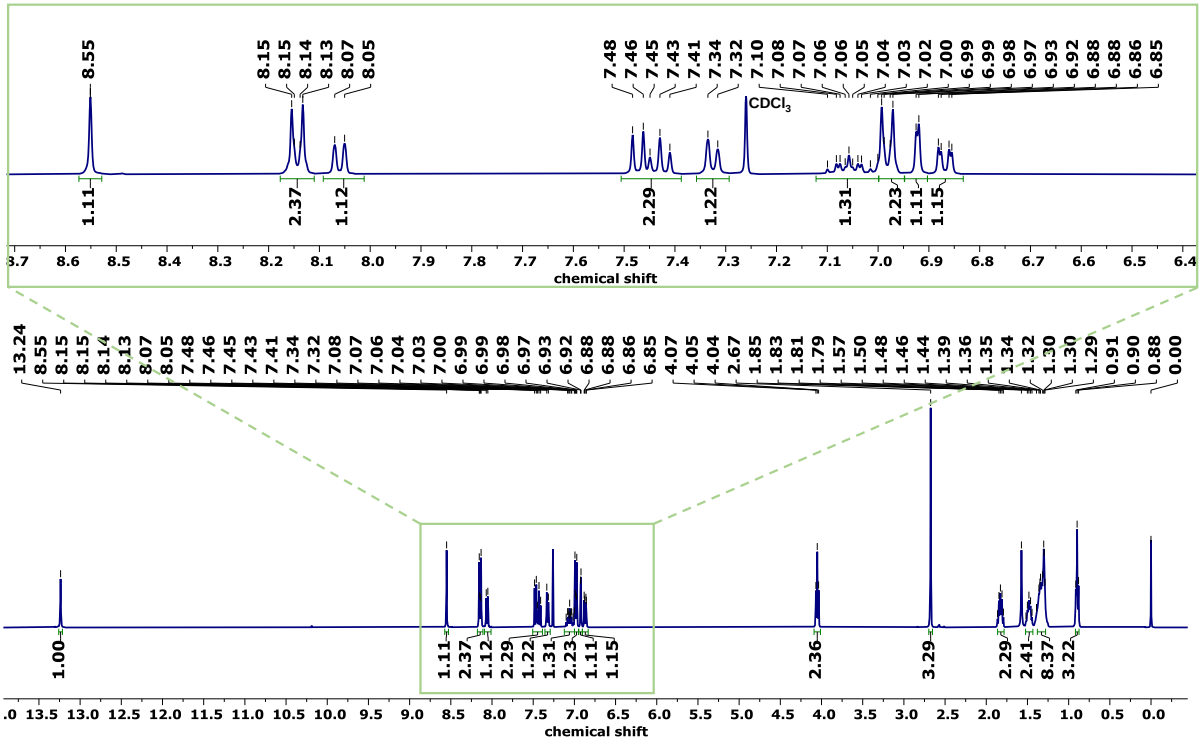

Fig. S1 ^{1}H NMR Spectra of **F4-8a.**

^{1}H NMR (400 MHz, $CDCl_3$, δ in ppm) δ = 13.24 (s, 1H, -OH), 8.55 (s, 1H, -CH=N-), 8.15 - 8.13 (m, 2H, Ar-H), 8.06 (d, *J* = 7.8 Hz, 1H, Ar-H), 7.48 - 7.41 (m, 2H, Ar-H), 7.34 - 7.32 (m, 1H, Ar-H), 7.10 - 7.02 (m, 1H, Ar-H), 7.00 - 6.97 (m, 2H, Ar-H), 6.92 (d, *J* = 2.2 Hz, 1H, Ar-H), 6.88 - 6.85 (m, 1H, Ar-H), 4.05 (t, 2H, -O-CH_2-), 2.67 (s, 3H, -CH_3 of core), 1.85 - 1.79 (m, 2H), 1.50 - 1.44 (m, 2H), 1.39 - 1.29 (m, 8H), 0.90 (t, 3H).

^{13}C {^{1}H} NMR (100 MHz, $CDCl_3$, δ in ppm) δ = 164.35, 163.77, 163.37, 163.03, 162.55, 155.35, 149.58, 147.38, 145.77, 135.17, 133.45, 132.43, 129.35, 128.30, 126.94, 123.67, 121.08, 117.03, 114.39, 113.46, 110.78, 103.34, 68.39, 31.82, 29.34, 29.24, 29.10, 26.00, 22.68, 15.44, 14.13.

FT-IR (cm^{-1}): 2918, 2852 (C-H stretching of alkyl groups), 1728 (C=O stretching of ester), 2354, 1610 (C=N of imine linkage), 1526, 1264, 1169, 1067, 753.

UV-visible absorption peaks (nm): 278, 339

Compound F4-12a

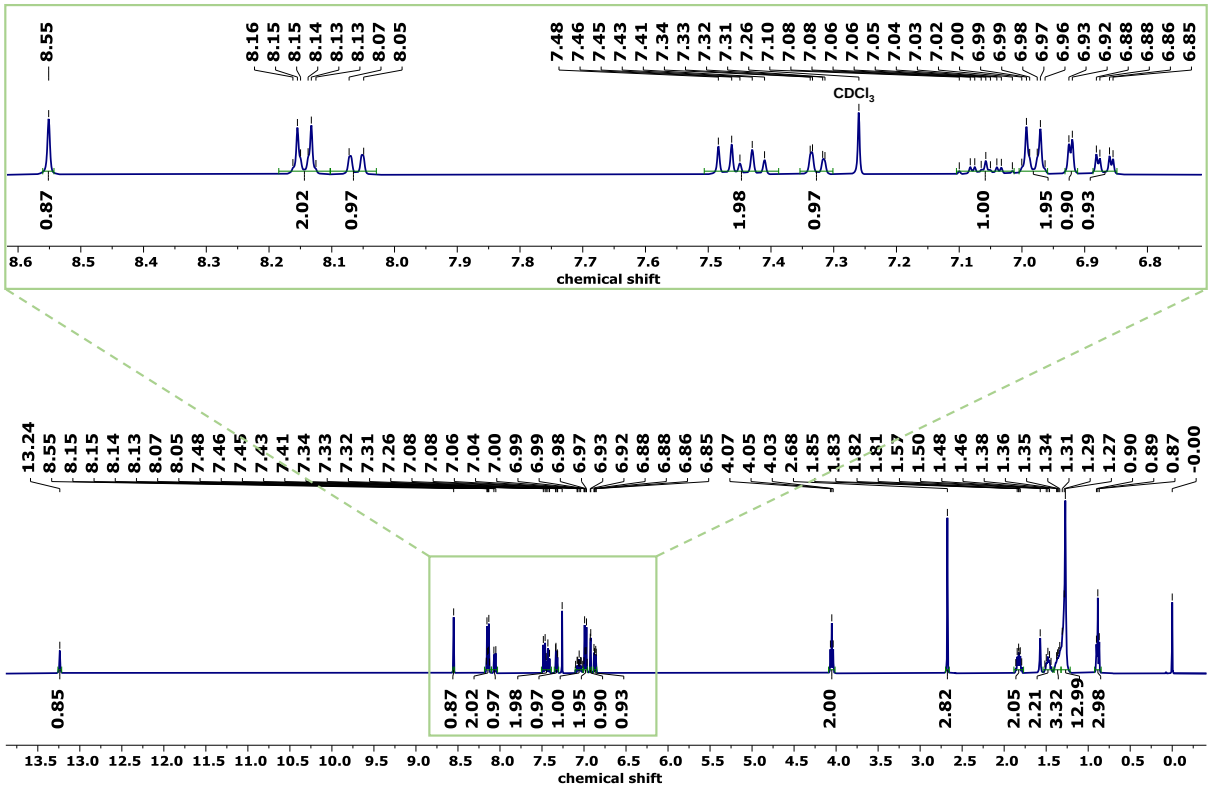

Fig. S2 ^{1}H NMR Spectra of **F4-12a.**

^{1}H NMR (400 MHz, $CDCl_3$, δ in ppm) δ = 13.24 (s, 1H, -OH), 8.55 (s, 1H, -CH=N-), 8.16 - 8.13 (m, 2H, Ar-H), 8.06 (d, *J* = 7.8 Hz, 1H, Ar-H), 7.48 - 7.41 (m, 2H, Ar-H), 7.34 - 7.31 (m, 1H, Ar-H), 7.10 - 7.02 (m, 1H, Ar-H), 7.00 - 6.96 (m, 2H, Ar-H), 6.92 (d, *J* = 2.2 Hz, 1H, Ar-H), 6.88 - 6.85 (m, 1H, Ar-H), 4.05 (t, 2H, -O-CH_2-), 2.68 (s, 3H, -CH_3 of core), 1.85 - 1.81 (m, 2H), 1.50 - 1.46 (m, 2H), 1.38 - 1.34 (m, 3H), 1.31 - 1.27 (m, 13H), 0.89 (t, 3H).

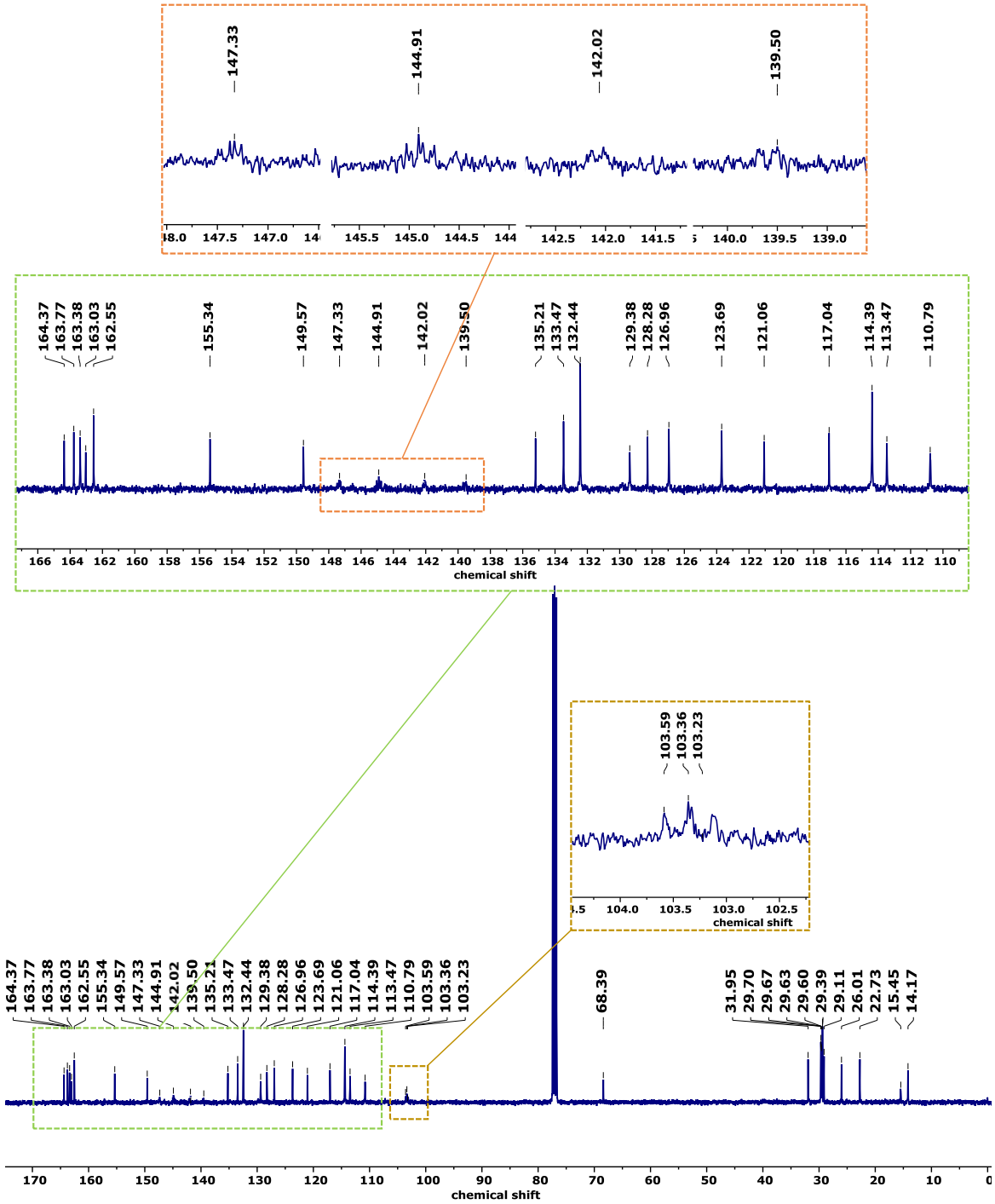

Fig. S3 ^{13}C {^{1}H} NMR Spectra of **F4-12a** (representative compound).

^{13}C {^{1}H} NMR (100 MHz, $CDCl_3$, δ in ppm) δ = 164.37, 163.77, 163.38, 163.03, 162.55, 155.34, 149.57, (147.33, 144.91, 142.02, 139.50; C atoms bonded to F), 135.21, 133.47, 132.44, 129.38, 128.28, 126.96, 123.69, 121.06, 117.04, 114.39, 113.47, 110.79, (103.59, 103.36, 103.23; aromatic C in fluorinated ring), 68.39, 31.95, 29.70, 29.67, 29.63, 29.60, 29.39, 29.11, 26.01, 22.73, 15.45, 14.17.

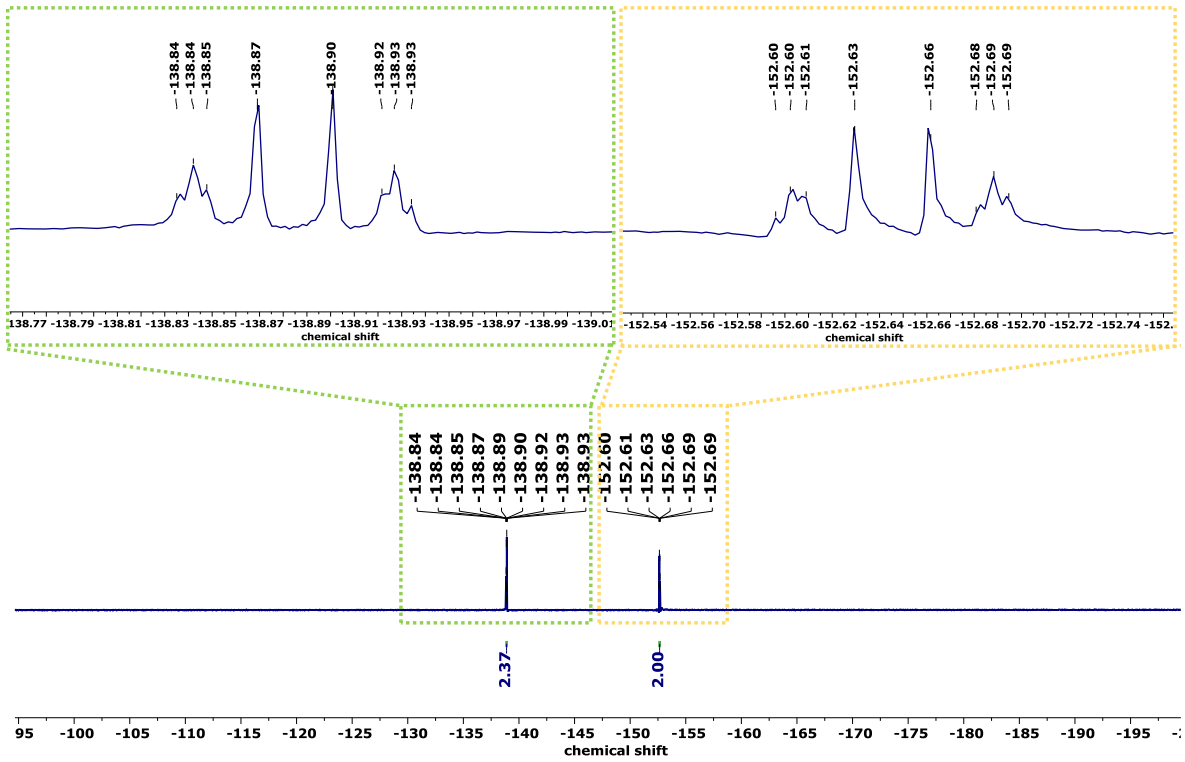

Fig. S4 $^{19}F\{^{1}H\}$ NMR Spectra of **F4-12a** (representative compound).

$^{19}F\{^{1}H\}$ NMR (377 MHz, $CDCl_3$, δ in ppm) -138.84 – -138.93 (m), -152.60 – -152.69 (m)

FT-IR (cm^{-1}): 2919, 2852 (C-H stretching of alkyl groups), 1727 (C=O stretching of ester), 2354, 1610 (C=N of imine linkage), 1525, 1264, 1166, 1067, 752.

UV-visible absorption peaks (nm): 279, 339

Compound F4-14a

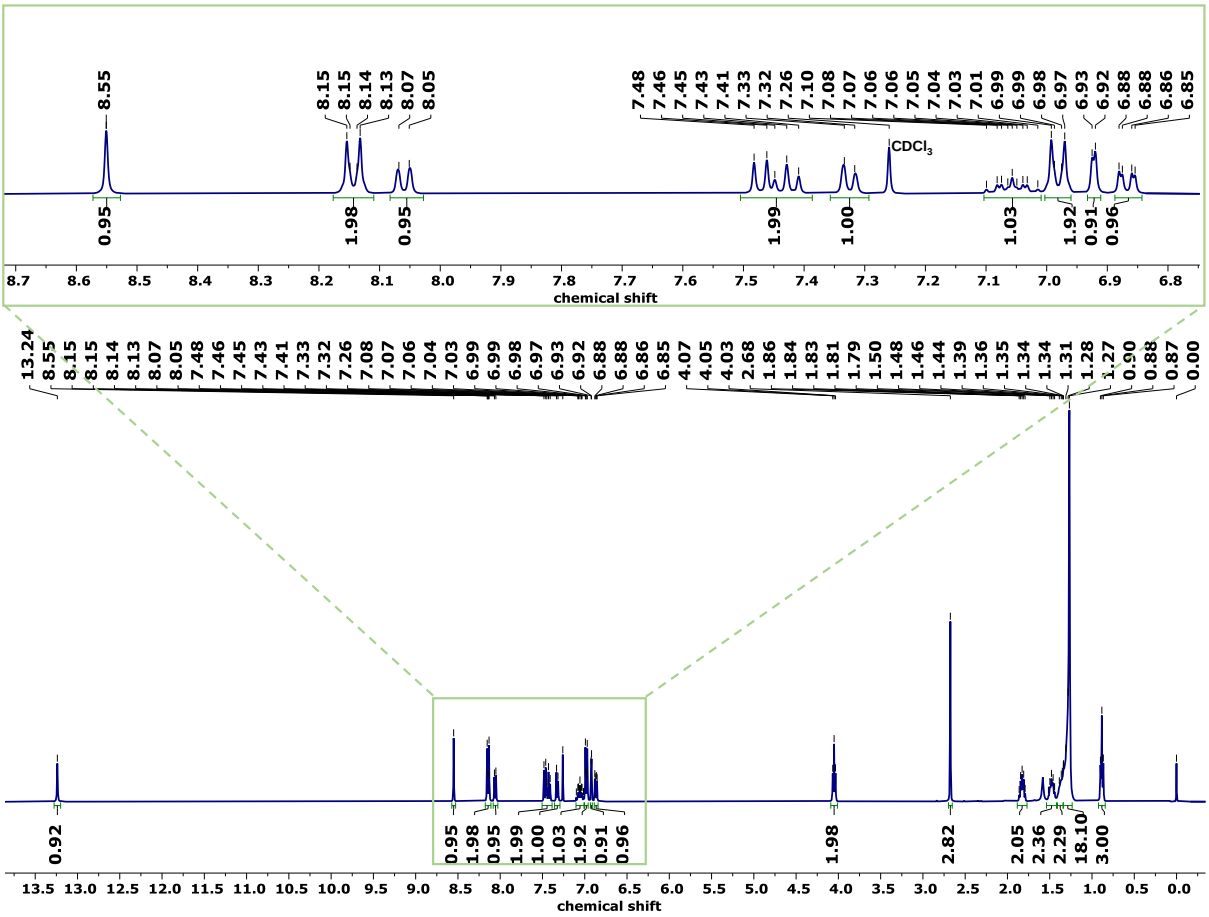

Fig. S5 ^{1}H NMR Spectra of **F4-14a.**

^{1}H NMR (400 MHz, $CDCl_3$, δ in ppm) δ = 13.24 (s, 1H, -OH), 8.55 (s, 1H, -CH=N-), 8.15 - 8.13 (m, 2H, Ar-H), 8.06 (d, *J* = 7.8 Hz, 1H, Ar-H), 7.48 - 7.41 (m, 2H, Ar-H), 7.33 - 7.32 (m, 1H, Ar-H), 7.10 - 7.01 (m, 1H, Ar-H), 6.99 - 6.97 (m, 2H, Ar-H), 6.92 (d, *J* = 2.2 Hz, 1H, Ar-H), 6.88 - 6.85 (m, 1H, Ar-H), 4.05 (t, 2H, -O-CH_2-), 2.68 (s, 3H, -CH_3 of Core), 1.86 - 1.79 (m, 2H), 1.50 - 1.44 (m, 2H), 1.39 - 1.34 (m, 2H), 1.34 - 1.27 (m, 18H), 0.88 (t, 3H).

^{13}C {^{1}H} NMR (100 MHz, $CDCl_3$, δ in ppm) δ = 164.35, 163.77, 163.37, 163.03, 162.55, 155.35, 149.58, 144.86, 135.17, 133.45, 132.43, 129.35, 128.30, 126.94, 123.67, 121.07, 117.03, 114.39, 113.45, 110.78, 103.32, 68.39, 31.95, 29.71, 29.68, 29.61, 29.58, 29.38, 29.10, 25.99, 22.72, 15.47, 14.15.

FT-IR (cm^{-1}): 2916, 2851 (C-H stretching of alkyl groups), 1727 (C=O stretching of ester), 2353, 1611 (C=N of imine linkage), 1526, 1263, 1169, 1067, 752.

UV-visible absorption peaks (nm): 282, 339

Compound F4-16a

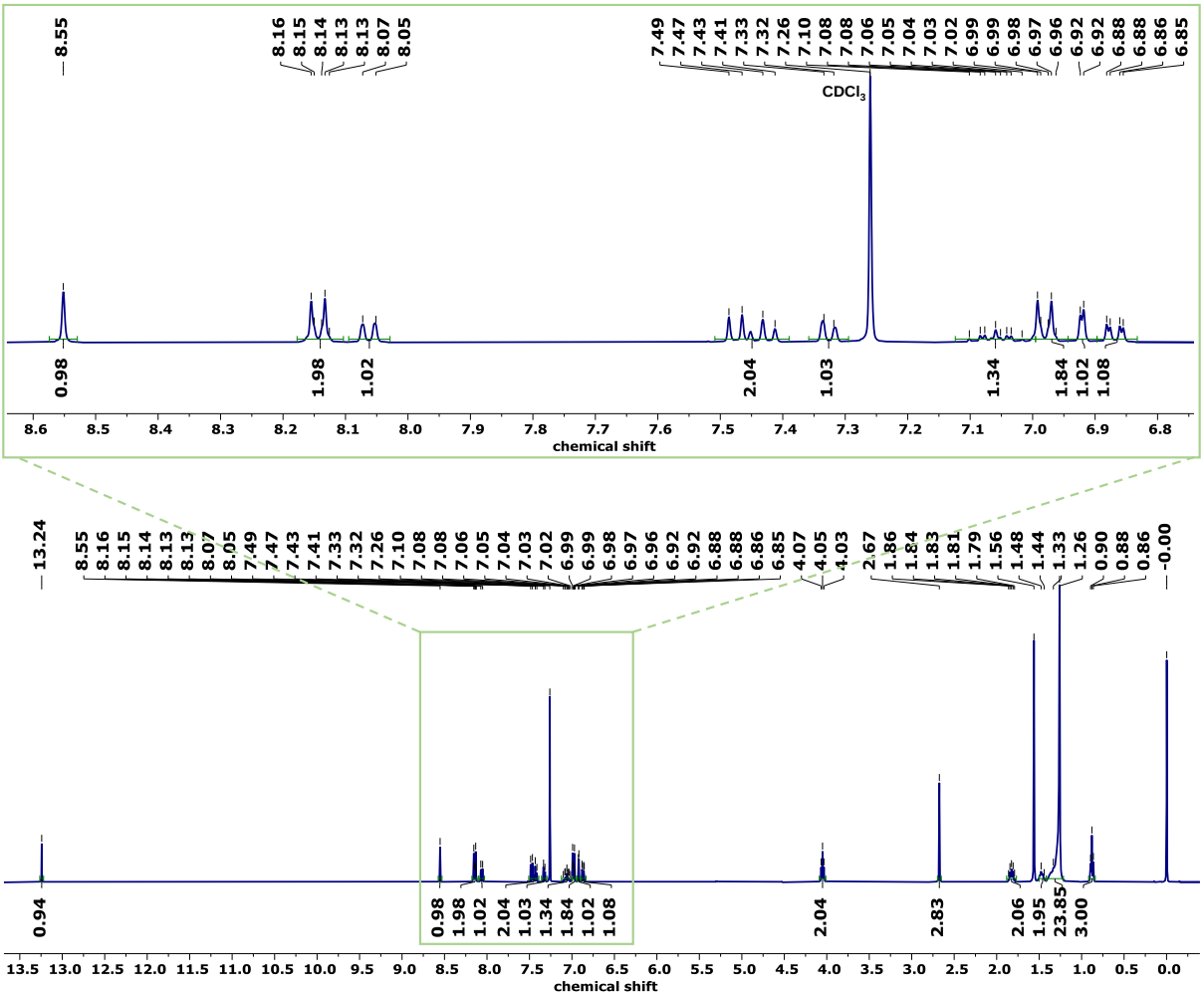

Fig. S6 ^{1}H NMR Spectra of **F4-16a.**

^{1}H NMR (400 MHz, $CDCl_3$, δ in ppm) δ = 13.24 (s, 1H, -OH), 8.55 (s, 1H, -CH=N-), 8.16 - 8.13 (m, 2H, Ar-H), 8.06 (d, *J* = 7.8 Hz, 1H, Ar-H), 7.49 - 7.41 (m, 2H, Ar-H), 7.33 - 7.32 (m, 1H, Ar-H), 7.10 - 7.02 (m, 1H, Ar-H), 6.99 - 6.96 (m, 2H, Ar-H), 6.92 (d, *J* = 2.2 Hz, 1H, Ar-H), 6.88 - 6.85 (m, 1H, Ar-H), 4.05 (t, 2H, -O-CH_2-), 2.67 (s, 3H, -CH_3 of Core), 1.86 - 1.79 (m, 2H), 1.48 - 1.44 (m, 2H), 1.33 - 1.26 (m, 24H), 0.88 (t, 3H).

^{13}C {^{1}H} NMR (100 MHz, $CDCl_3$, δ in ppm) δ = 164.36, 163.77, 163.37, 163.03, 162.54, 155.34, 149.56, 147.33, 135.19, 133.46, 132.43, 129.37, 128.28, 126.95, 123.68, 121.06, 117.04, 114.38, 113.46, 110.78, 103.34, 68.39, 31.96, 29.73, 29.69, 29.62, 29.59, 29.40, 29.11, 26.00, 22.73, 15.45, 14.16.

FT-IR (cm^{-1}): 2920, 2849 (C-H stretching of alkyl groups), 1728 (C=O stretching of ester), 2354, 1610 (C=N of imine linkage), 1526, 1262, 1169, 1067, 754.

UV-visible absorption peaks (nm): 278, 339

Compound F4-18a

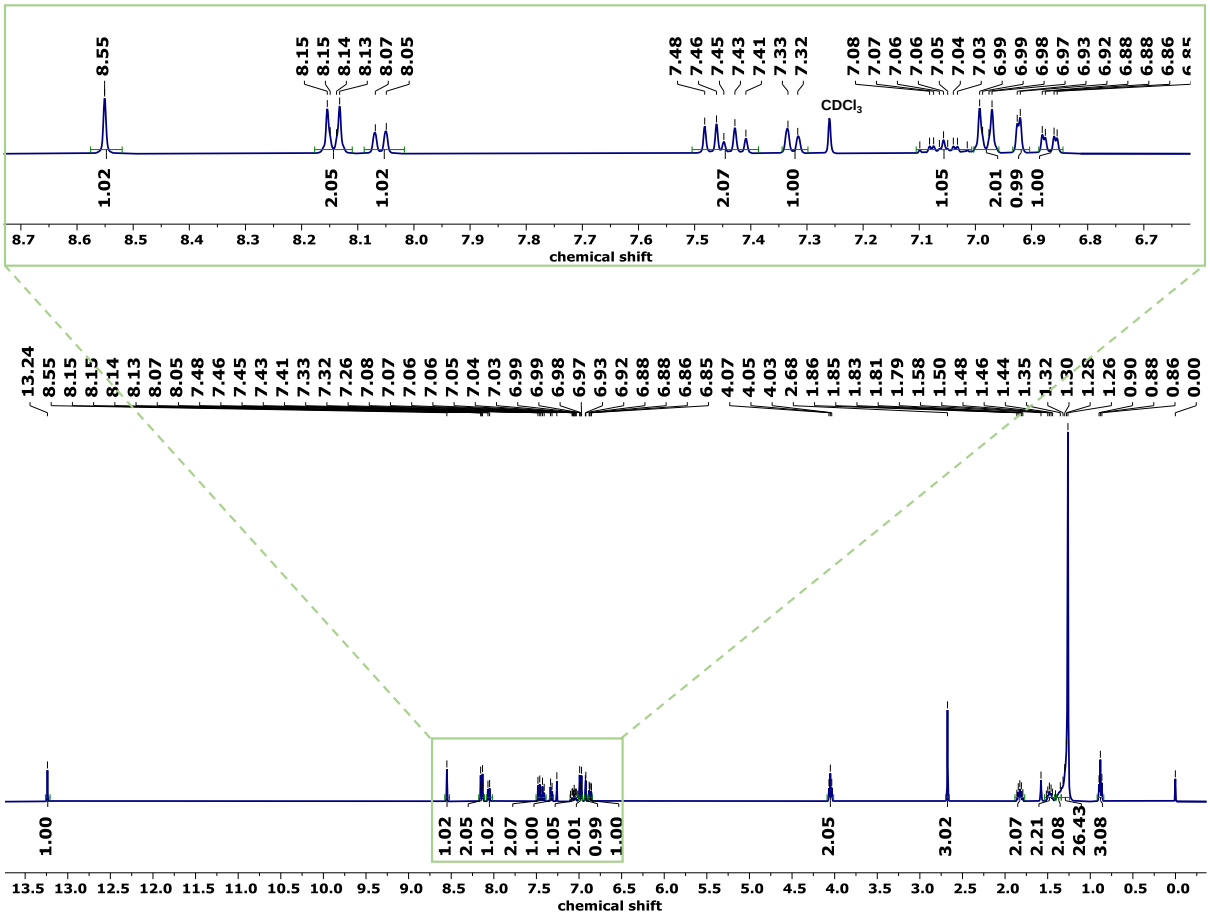

Fig. S7 ^{1}H NMR Spectra of **F4-18a.**

^{1}H NMR (400 MHz, $CDCl_3$, δ in ppm) δ = 13.24 (s, 1H, -OH), 8.55 (s, 1H, -CH=N-), 8.15 - 8.13 (m, 2H, Ar-H), 8.06 (d, *J* = 7.8 Hz, 1H, Ar-H), 7.48 - 7.41 (m, 2H, Ar-H), 7.33 - 7.32 (m, 1H, Ar-H), 7.08 - 7.03 (m, 1H, Ar-H), 6.99 - 6.97 (m, 2H, Ar-H), 6.92 (d, *J* = 2.2 Hz, 1H, Ar-H), 6.88 - 6.85 (m, 1H, Ar-H), 4.05 (t, 2H, -O-CH_2), 2.68 (s, 3H, -CH_3 of Core), 1.86 - 1.79 (m, 2H), 1.50 - 1.44 (m, 2H), 1.35 - 1.32 (m, 2H), 1.30 - 1.26 (m, 26H), 0.88 (t, 3H).

^{13}C {^{1}H} NMR (100 MHz, $CDCl_3$, δ in ppm) δ = 164.35, 163.77, 163.37, 163.02, 162.55, 155.36, 149.58, 135.17, 133.45, 132.42, 129.35, 128.30, 126.94, 123.66, 121.08, 117.03, 114.38, 113.46, 110.78, 103.33, 68.39, 31.95, 29.72, 29.68, 29.61, 29.58, 29.39, 29.10, 26.00, 22.72, 15.44, 14.15.

FT-IR (cm^{-1}): 2918, 2851 (C-H stretching of alkyl groups), 1728 (C=O stretching of ester), 2354, 1610 (C=N of imine linkage), 1524, 1262, 1169, 1067, 753.

UV-visible absorption peaks (nm): 278, 339

3. Polarized Optical Microscopy

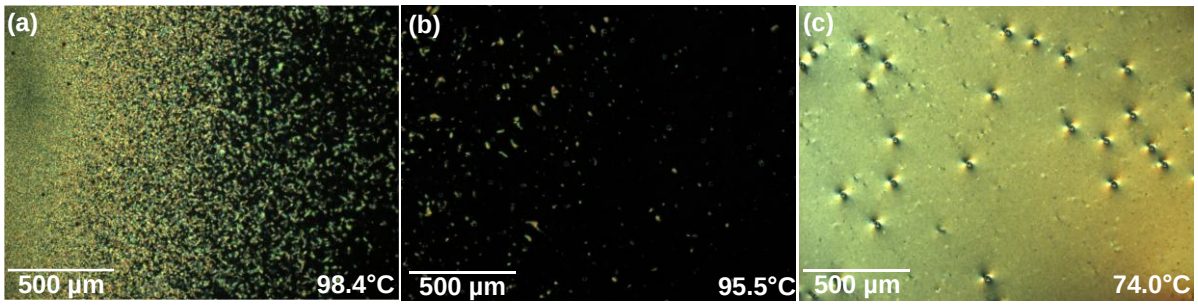

Fig. S8 POM textures (under crossed polarizers) for **F4-8a** (a-c) showing the transition from N to SmC phase in 18.3 µm homeotropic cell, observed at a cooling rate of 10 °C min^{-1}.

F4-8a, on a standard glass slide, exhibits an isotropic to N phase transition at 108 °C, followed by a transition to a homeotropic dark texture. Subsequently, the SmC phase emerges at 78.4 °C, followed by crystallization at 69.2 °C. In a homeotropic cell with a thickness of 18.3 µm, the isotropic to N transition is observed at 101.5 °C, followed by a homeotropic dark texture. At 81.9 °C, the SmC phase emerges, with crystallization occurring around 68.5 °C (Fig. S8 (a-c)).

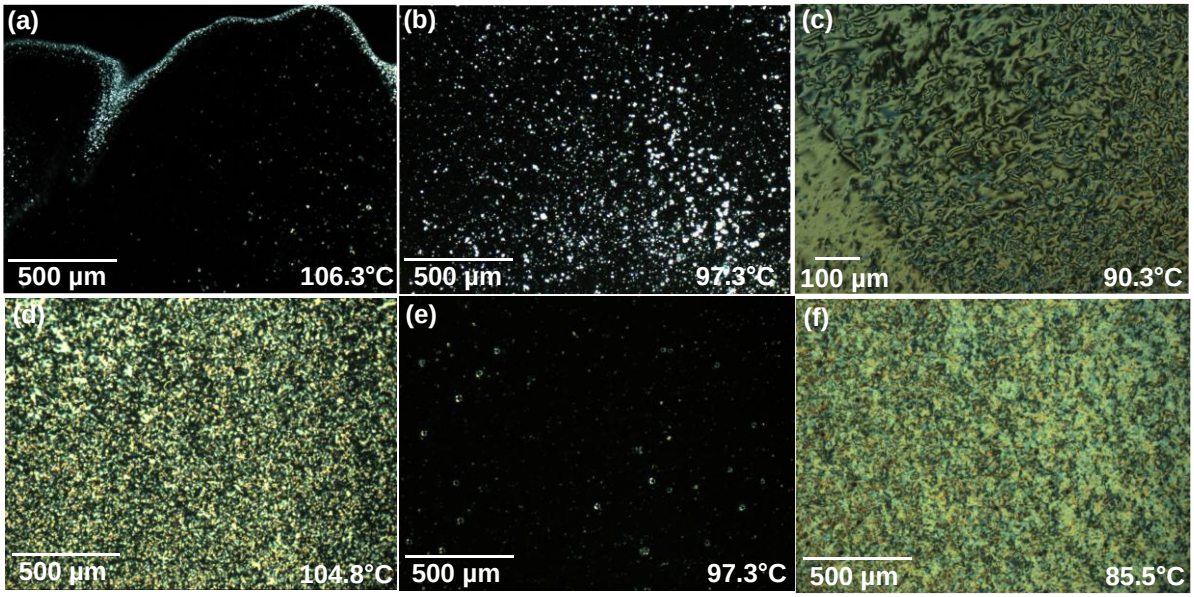

Fig. S9 POM textures (under crossed polarizers) for **F4-12a** (a-c) on a glass slide with a coverslip (cooling rate 5 °C min^{-1}); (d-f) in 18.3 µm homeotropic cell, observed at a cooling rate of 10 °C min^{-1}.

On a standard glass slide, **F4-12a** exhibits an isotropic to N transition around 106.2 °C, followed by a transition to a homeotropic-like orientation. Subsequently, another phase transition (to SmC phase) occurs at 96.3 °C, with crystallization observed at 61 °C. In a homeotropic cell with a thickness of 18.3 µm, the isotropic to N transition is observed at 104.8 °C, followed by a homeotropic dark texture. At 94.9 °C, the SmC phase emerges, with crystallization occurring around 57.7 °C (Fig. S9). POM textures under planar alignment conditions are provided in **Fig. S18**.

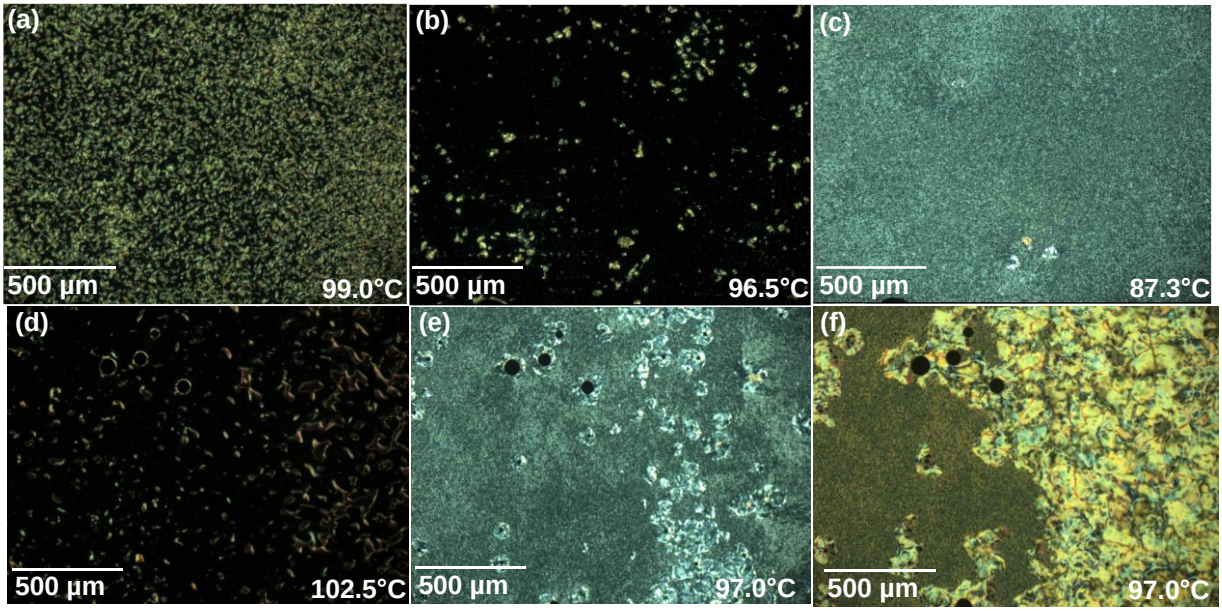

Fig. S10 POM textures (under crossed polarizers) for **F4-14a** (a-c) on a glass slide with a coverslip (cooling rate 5 °C min^{-1}); (d-f) in 18.3 µm homeotropic cell, observed at a cooling rate of 10 °C min^{-1}.

The compound **F4-14a**, when observed on a glass slide, exhibits birefringence upon cooling from isotropic state at 100.3 °C (to N phase), which transforms into a homeotropic-like dark texture. Some regions show changes in birefringent spots near 98 °C. At 90.3 °C, a transition to the SmC phase occurs, and the sample crystallizes at 63.5 °C. In a homeotropic cell with a thickness of 18.3 µm, the N phase appears at 103.5 °C, gradually transitioning to a homeotropic-like texture, and then displaying SmC at 98 °C (Fig. S10). POM textures under planar alignment conditions are provided in **Fig. S19**.

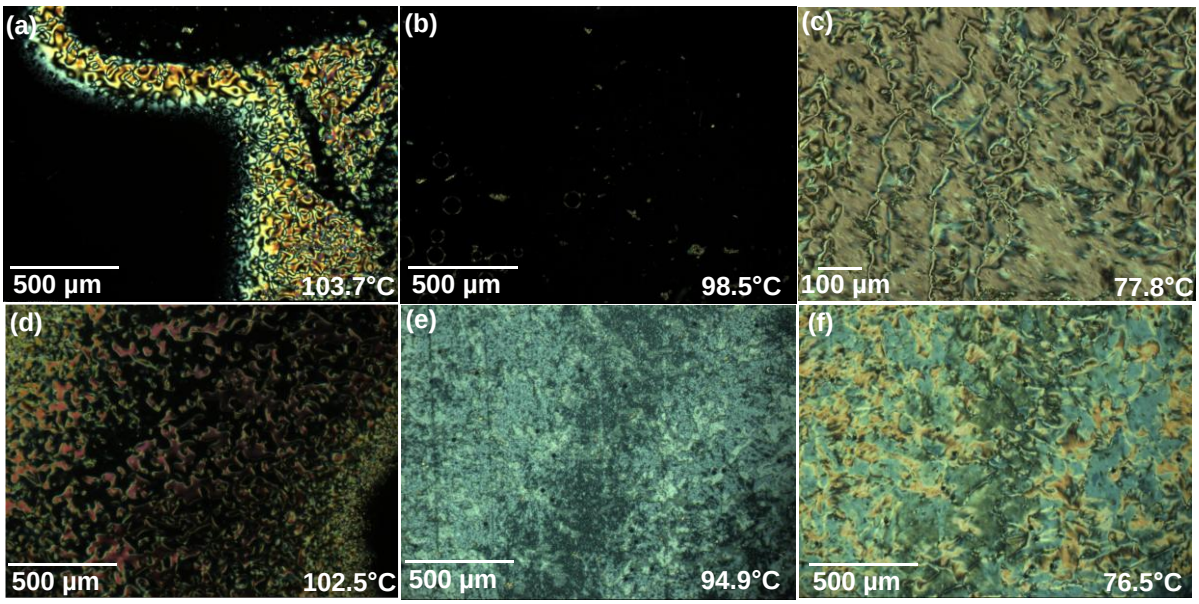

Fig. S11 POM textures (under crossed polarizers) for **F4-16a** (a-c) on a glass slide with a

coverslip (cooling rate 5 °C min^{-1}); (d-f) in 18.3 µm homeotropic cell, observed at a cooling rate of 10 °C min^{-1}.

For the **F4-16a** sample, transitions were observed under various conditions. On a glass slide, the N phase transition occurred at 103.7 °C (became dark on cooling), followed by the SmC phase transition at 97.9 °C, and crystallization at 71.9 °C. In a homeotropic cell with an 18.3 µm thickness, the transitions occurred as follows: 103.4 °C for the Iso-N, 97.4 °C for the N-SmC phase, and 68.6 °C for crystallization (Fig. S11).

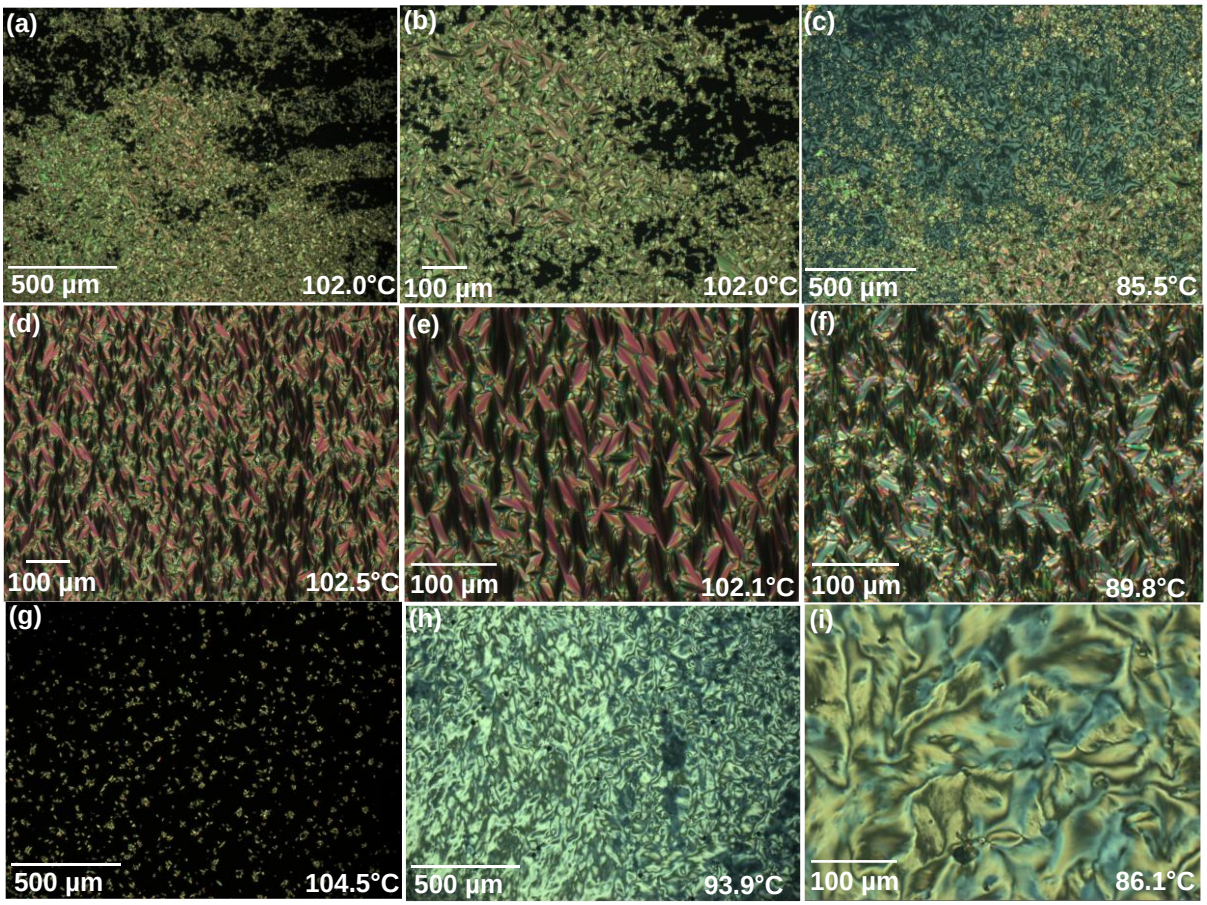

Fig. S12 POM textures (under crossed polarizers) for **F4-18a** (a-c) on a glass slide with a coverslip (cooling rate 5 °C min^{-1}); (d-f) in 7.7 µm planar cell and (g-i) in 18.3 µm homeotropic cell, observed at a cooling rate of 10 °C min^{-1}.

For the **F4-18a** sample, as observed on a glass slide, the LC phase forms at 104.8 °C, displaying focal conic textures with some homeotropic regions. Upon further cooling, both focal conic textures and underlying Schlieren-like textures of SmC are observed. Crystallization occurs at 78.6 °C. However, in a planar cell with a thickness of 7.7 µm, characteristic focal conic textures appear at 105.4 °C. In a homeotropic cell with a thickness of 18.3 µm, transient nematic-like textures appear at 104.5 °C, which then convert to Schlieren textures of the SmC phase at 98.6 °C before crystallizing at 76.5 °C (Fig. S12).

4. Differential Scanning Calorimetry

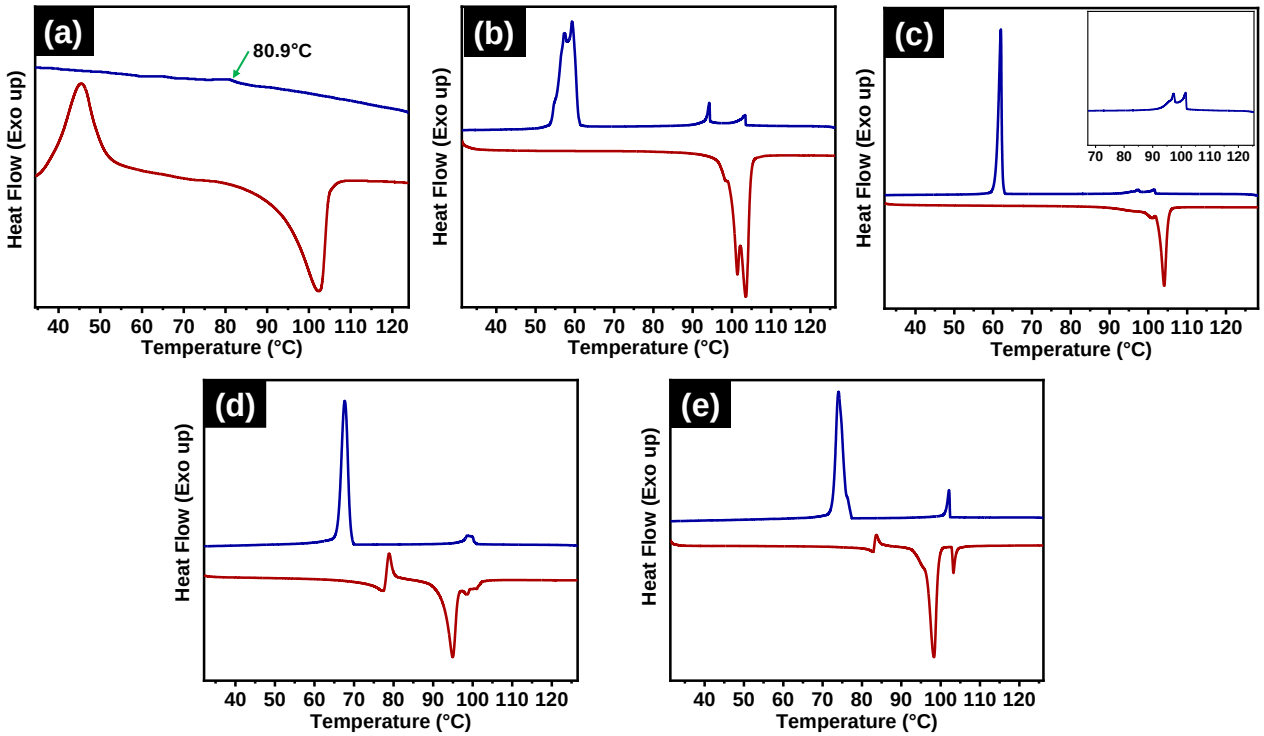

Fig. S13 DSC thermograms obtained for **F4-na** compounds (a) n = 8 (b) n = 12 (c) n = 14 (d) n = 16 (e) n = 18, at a rate of 5 °C min^{-1} (Y-axis denote exothermic peaks up, red curve represents heating and blue curve represent cooling cycle).

5. Small-angle/Wide-angle X-Ray Scattering

The *d*-spacing can be calculated using Bragg's equation: $\mathbf{2}\boldsymbol{d}\ \boldsymbol{sin}\boldsymbol{\theta} = \mathbf{n}\boldsymbol{\lambda}$, where θ is the peak position determined from intensity vs. 2θ plots (where 2θ is known as scattering angle), λ is the wavelength of the X-ray beam (λ = 1.542 Å), and n = 1 for first-order diffraction. Additionally, the tilt angle (β) relative to the layer normal can be calculated using cos β = *d*/L where L is the molecular length of the compound, obtained from DFT calculations.

The correlation length (ξ), representing the degree of order within the mesophases, has been calculated using $\xi = k.2\pi/(\Delta q)$.[2] Here, k is the shape factor typically valued at 0.89 or q is the scattering wave vector ($q = 4\pi.\sin\theta/\lambda$) and Δq is the broadening in q at half the maximum intensity (FWHM). The number of correlated units is obtained by dividing the correlation length by the corresponding *d*-spacing (ξ/*d*), which indicates how many units are aligned to reflect that correlation length.[2]

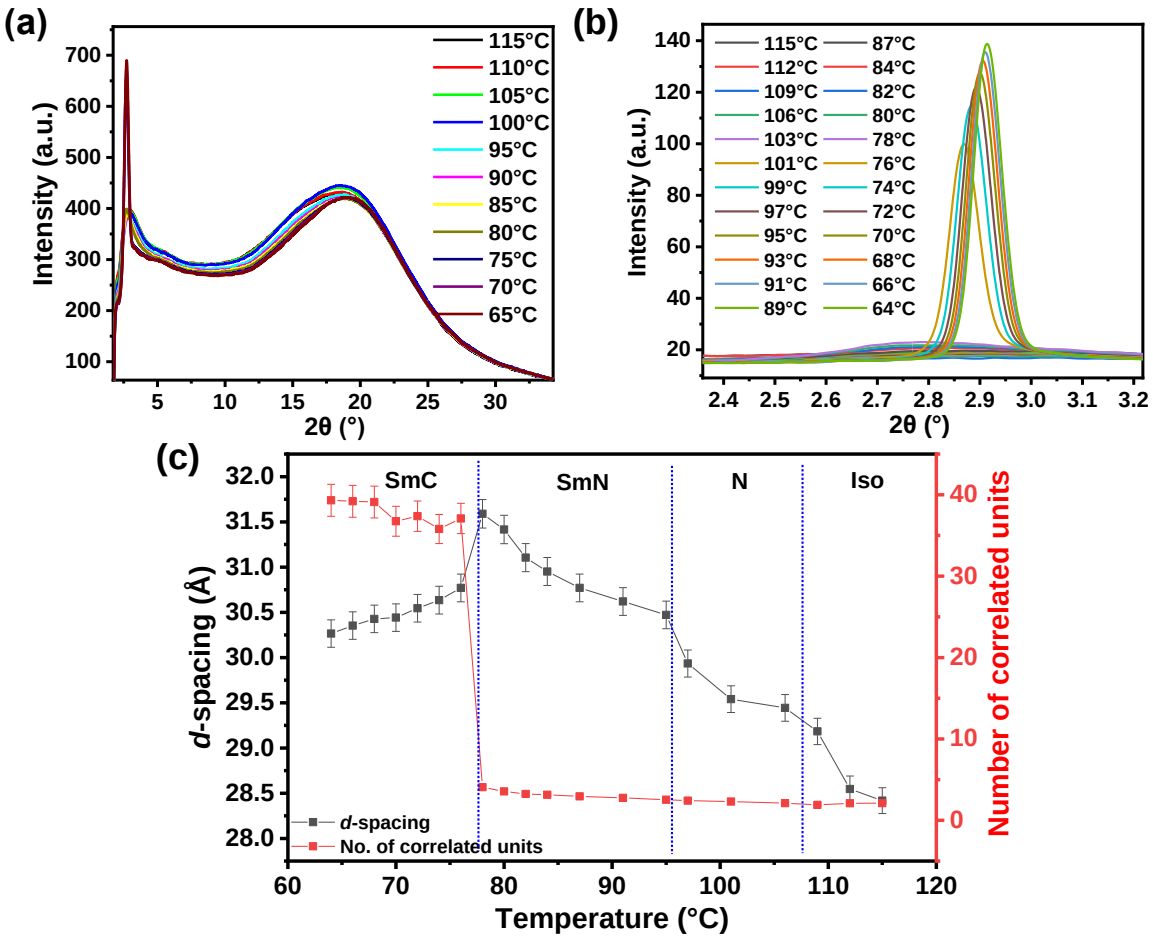

Fig. S14 (a) WAXS data showing temperature-dependent intensity vs. 2θ (in degree) profiles for **F4-8a**, illustrating one small-angle peak and one diffuse wide-angle peak (b) Temperature variation of the small-angle peak (SAXS data) and (c) Variation of *d*-spacing and correlation length with respect to temperature, demonstrating different phases observed in Compound **F4-8a**.

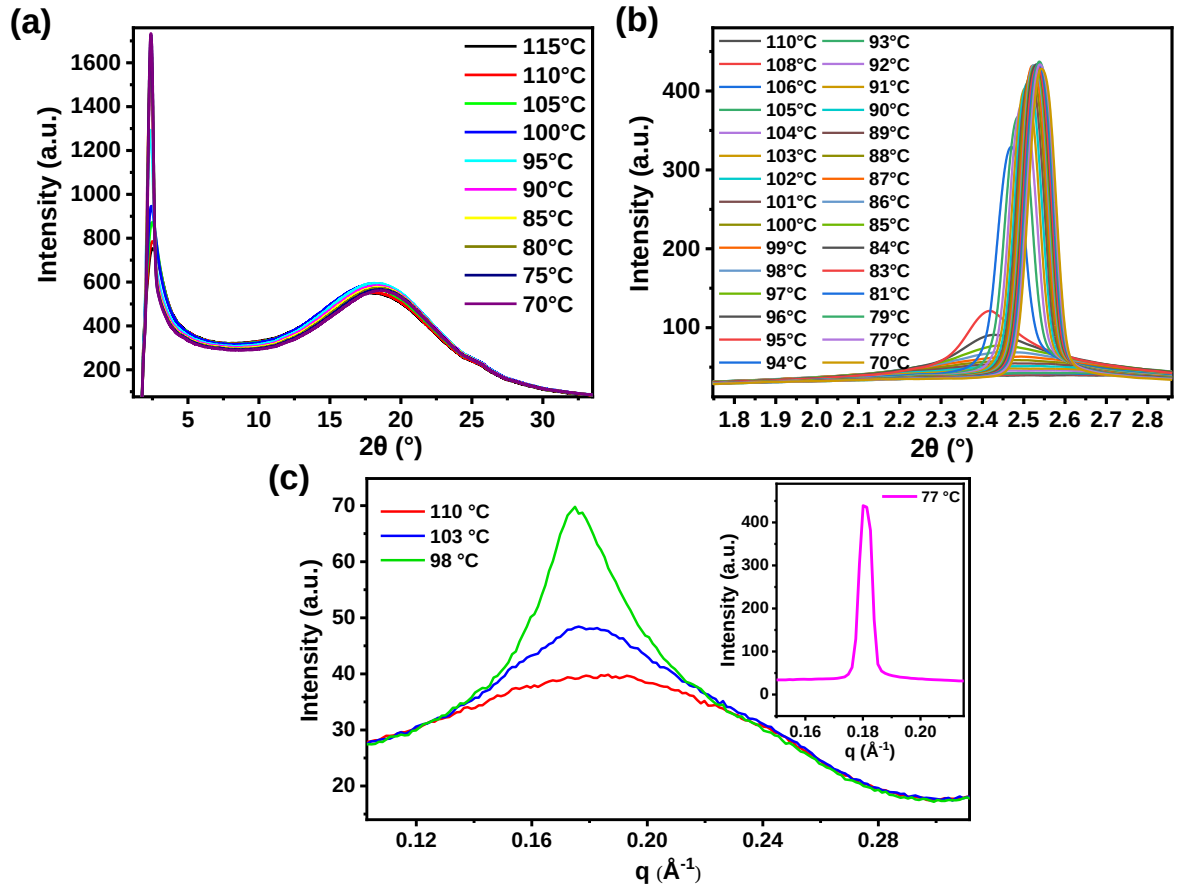

Fig. S15 (a) WAXS data showing temperature-dependent intensity vs. 2θ (in degree) profiles for **F4-12a**, illustrating one small-angle peak and one diffuse wide-angle peak (b) Temperature variation of the small-angle peak (SAXS data) and (c) SAXS peaks expressed in q-space at different phases: Isotropic (110 °C), N (103 °C), N_{cyb} (98 °C), and SmC (77 °C) for **F4-12a**.

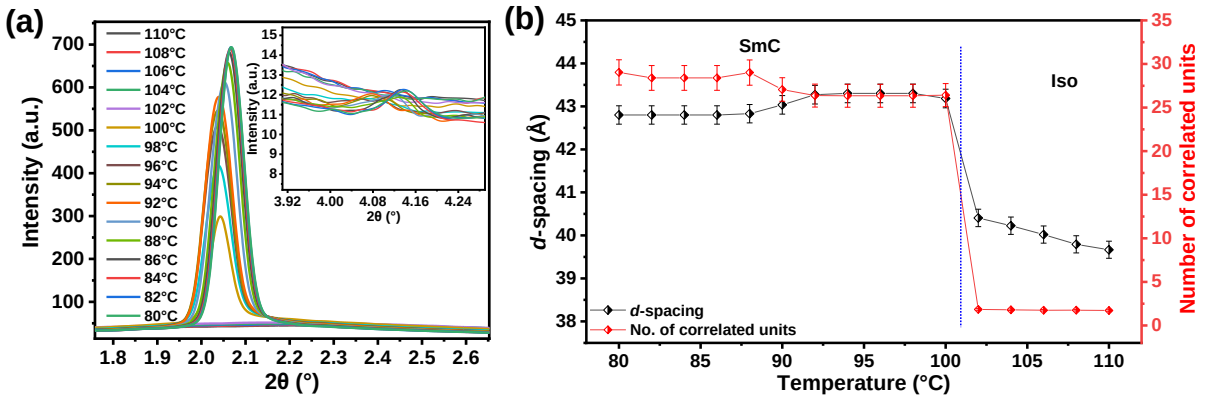

Fig. S16 (a) Temperature variation of the small-angle peak (SAXS data) and (b) Variation of *d*-spacing and correlation length with respect to temperature, demonstrating different phases observed in Compound **F4-18a**.

Table S1. Parameters calculated from SAXS/WAXS data for F4-8a (cooling cycle).

Temperature (°C)	*d*-spacing ± 0.15 (Å)	Correlation length (Å)	No. of correlated units	Tilt angle with layer normal (°)	Phase
64	30.26	1189.79 ± 59.49	39.31 ± 1.97	20.11 ± 1.01	SmC
66	30.35	1189.79 ± 59.49	39.20 ± 1.96	19.65 ± 0.98	SmC
68	30.43	1189.79 ± 59.49	39.10 ± 1.96	19.26 ± 0.98	SmC
70	30.44	1118.41 ± 55.92	36.74 ± 1.84	19.18 ± 0.96	SmC
72	30.54	1141.23 ± 57.06	37.36 ± 1.87	18.61 ± 0.93	SmC
74	30.64	1096.48 ± 54.82	35.79 ± 1.79	18.10 ± 0.91	SmC
76	30.77	1141.23 ± 57.06	37.09 ± 1.85	17.31 ± 0.87	SmC
78	31.59	128.85 ± 6.44	4.08 ± 0.20		N_{cyb}
80	31.42	111.40 ± 5.57	3.54 ± 0.18		N_{cyb}
82	31.11	100.94 ± 5.05	3.24 ± 0.16		N_{cyb}
84	30.95	97.25 ± 4.86	3.14 ± 0.16		N_{cyb}
87	30.77	90.63 ± 4.53	2.95 ± 0.15		N_{cyb}
91	30.62	84.60 ± 4.23	2.76 ± 0.14		N_{cyb}
95	30.47	77.13 ± 3.86	2.53 ± 0.13		N
97	29.93	72.53 ± 3.63	2.42 ± 0.12		N
101	29.54	68.28 ± 3.41	2.31 ± 0.12		N
106	29.44	62.00 ± 3.10	2.11 ± 0.11		N
109	29.18	55.59 ± 2.78	1.91 ± 0.10		Iso
112	28.55	59.87 ± 3.00	2.10 ± 0.11		Iso
115	28.42	59.87 ± 3.00	2.11 ± 0.11		Iso

Table S2. Parameters calculated from SAXS/WAXS data for F4-12a (cooling cycle).

Temperature (°C)	*d*-spacing ± 0.15 (Å)	Correlation length (Å)	No. of correlated units	Tilt angle with layer normal (°)	Phase
70	34.62	1055.10 ± 52.76	30.48 ± 1.52	21.86 ± 1.09	SmC
77	34.71	1055.10 ± 52.76	30.39 ± 1.52	21.46 ± 1.07	SmC
81	34.83	1035.56 ± 51.78	29.73 ± 1.49	20.97 ± 1.05	SmC
83	34.85	1096.48 ± 54.82	31.46 ± 1.57	20.89 ± 1.04	SmC
85	34.94	1075.39 ± 53.77	30.77 ± 1.54	20.47 ± 1.02	SmC
87	35.00	1096.48 ± 54.82	31.32 ± 1.57	20.21 ± 1.01	SmC
89	35.12	1118.40 ± 55.92	31.84 ± 1.59	19.68 ± 0.98	SmC
91	35.24	1096.48 ± 54.82	31.11 ± 1.56	19.13 ± 0.96	SmC
93	35.54	1075.39 ± 53.77	30.26 ± 1.51	17.68 ± 0.88	SmC
94	35.68	1075.39 ± 53.77	30.14 ± 1.51	16.95 ± 0.85	SmC
95	36.51	372.80 ± 18.64	10.21 ± 0.51		N_{cyb}
96	36.40	222.79 ± 11.14	6.12 ± 0.31		N_{cyb}
97	36.07	171.01 ± 8.55	4.74 ± 0.24		N_{cyb}
98	35.86	136.06 ± 6.80	3.79 ± 0.19		N_{cyb}
99	35.62	116.50 ± 5.82	3.27 ± 0.16		N_{cyb}
100	35.52	102.80 ± 5.14	2.89 ± 0.14		N
101	35.40	91.08 ± 4.55	2.57 ± 0.13		N
102	35.16	81.40 ± 4.07	2.31 ± 0.12		N
103	35.08	74.86 ± 3.74	2.13 ± 0.11		N
104	34.58	69.47 ± 3.47	2.01 ± 0.10		N
105	34.22	60.92 ± 3.05	1.78 ± 0.09		Iso
106	34.20	59.87 ± 2.99	1.75 ± 0.09		Iso
108	34.11	57.77 ±2.89	1.69 ± 0.08		Iso
110	34.00	56.77 ± 2.84	1.67 ± 0.08		Iso

Table S3. Parameters calculated from SAXS/WAXS data for F4-14a (cooling cycle).

Temperature (°C)	*d*-spacing ± 0.15 (Å)	Correlation length (Å)	No. of correlated units	Tilt angle with layer normal (°)	Phase
72	37.14	1141.23 ± 57.06	30.73 ± 1.54	21.42 ± 1.07	SmC
76	37.14	1141.23 ± 57.06	30.73 ±1.54	21.42 ± 1.07	SmC
80	37.14	1118.41 ± 55.92	30.12 ± 1.51	21.42 ± 1.07	SmC
83	37.14	1141.23 ± 57.06	30.73 ± 1.54	21.42 ± 1.07	SmC
86	37.29	1141.23 ±57.06	30.61 ± 1.53	20.81 ± 1.04	SmC
89	37.58	1165.01 ± 58.25	31.00 ± 1.55	19.60 ± 0.98	SmC
92	38.26	1055.10 ± 52.76	27.57 ± 1.38	16.41 ± 0.82	SmC
95	38.31	238.98 ± 11.95	6.24 ± 0.31		N_{cyb}
98	37.29	104.52 ± 5.23	2.80 ± 0.14		N_{cyb}
100	36.19	63.98 ± 3.20	1.77 ± 0.09		N
102	36.19	62.00 ± 3.10	1.71 ± 0.09		N
105	36.19	60.72 ± 3.04	1.68 ± 0.08		Iso
108	36.19	60.72 ± 3.04	1.68 ± 0.08		Iso
110	36.19	57.95 ± 2.90	1.60 ± 0.08		Iso

Table S4. Parameters calculated from SAXS/WAXS data for F4-16a (cooling cycle).

Temperature (°C)	*d*-spacing ± 0.15 (Å)	Correlation length (Å)	No. of correlated units	Tilt angle with layer normal (°)	Phase
76	39.69	1433.86 ± 71.69	36.12 ± 1.81	20.73 ± 1.04	SmC
78	39.69	1433.86 ± 71.69	36.12 ± 1.81	20.73 ± 1.04	SmC
80	39.69	1433.86 ± 71.69	36.12 ± 1.81	20.73 ± 1.04	SmC
82	39.69	1433.86 ± 71.69	36.12 ± 1.81	20.73 ± 1.04	SmC
84	39.69	1433.86 ± 71.69	36.12 ± 1.81	20.73 ± 1.04	SmC
86	39.69	1433.86 ± 71.69	36.12 ± 1.81	20.73 ± 1.04	SmC
88	39.87	1363.91 ± 68.20	34.21 ± 1.71	20.05 ± 1.00	SmC
90	39.92	1363.91 ± 68.20	34.17 ± 1.71	19.85 ± 0.99	SmC
92	40.02	1363.91 ±68.20	34.08 ± 1.70	19.44 ± 0.97	SmC
94	40.17	1331.44 ±66.57	33.14 ± 1.66	18.81 ± 0.94	SmC
96	40.35	1433.86 ± 71.69	35.53 ± 1.78	18.04 ± 0.90	SmC
98	40.85	1300.47 ± 65.02	31.83 ± 1.59	15.72 ± 0.79	SmC
100	41.07	1398.02 ± 69.90	34.04 ± 1.70	14.62 ± 0.73	SmC
102	40.54	173.67 ± 8.68	4.28 ± 0.21		N
104	38.67	77.45 ± 3.87	2.00 ± 0.10		Iso
106	38.26	73.29 ± 3.66	1.91 ± 0.10		Iso
108	37.96	72.81 ± 3.64	1.92 ± 0.10		Iso

Table S5. Parameters calculated from SAXS/WAXS data for F4-18a (cooling cycle).

Temperature (°C)	*d*-spacing ± 0.15 (Å)	Correlation length (Å)	No. of correlated units	Tilt angle with layer normal (°)	Phase
80	42.80	1242.67 ± 62.13	29.03 ± 1.45	17.99 ± 0.90	SmC
82	42.80	1215.66 ± 60.78	28.40 ± 1.42	17.99 ± 0.90	SmC
84	42.80	1215.66 ± 60.78	28.40 ± 1.42	17.99 ± 0.90	SmC
86	42.80	1215.66 ± 60.78	28.40 ± 1.42	17.99 ± 0.90	SmC
88	42.83	1242.67 ± 62.13	29.01 ± 1.4	17.86 ± 0.89	SmC
90	43.04	1165.00 ± 58.25	27.07 ± 1.35	16.99 ± 0.86	SmC
92	43.27	1141.23 ± 57.06	26.37 ± 1.32	15.93 ± 0.80	SmC
94	43.30	1141.23 ± 57.06	26.36 ± 1.32	15.79 ± 0.79	SmC
96	43.30	1141.23 ± 57.06	26.36 ± 1.32	15.79 ± 0.79	SmC
98	43.30	1141.23 ± 57.06	26.36 ± 1.32	15.79 ± 0.79	SmC
100	43.18	1141.23 ± 57.06	26.43 ± 1.32	15.79 ± 0.79	SmC
102	40.41	74.46 ± 3.72	1.84 ± 0.09		Iso
104	40.22	72.25 ± 3.61	1.80 ± 0.09		Iso
106	40.02	69.73 ± 3.49	1.74 ± 0.09		Iso
108	39.79	69.73 ± 3.49	1.75 ± 0.09		Iso
110	39.67	68.03 ± 3.40	1.72 ± 0.09		Iso

6. Structure-Property Relation

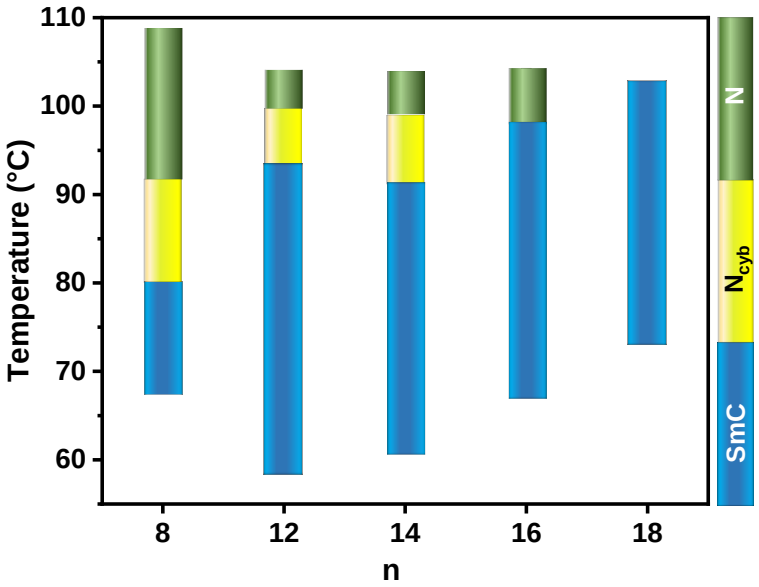

Fig. S17 Graphical representation of phases exhibited by various homologues of the **F4-na** series of compounds.

7. Birefringence Measurements

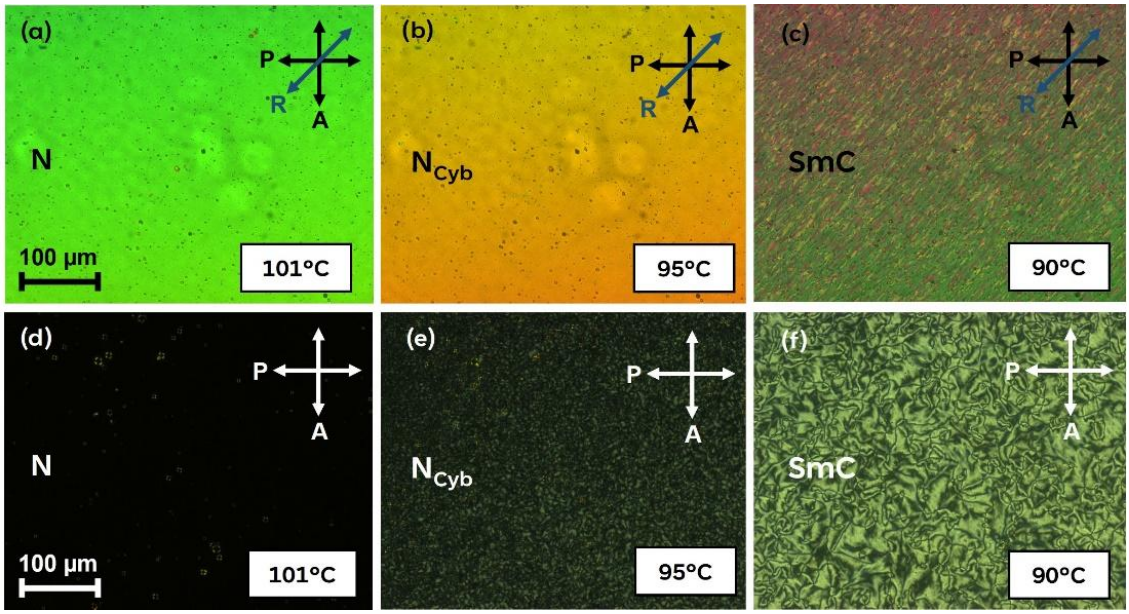

Fig. S18 POM micrographs of **F4-12a** at different temperatures in (a-c) a planar cell (antiparallel buffing) and (d-f) a homeotropic cell with a thickness of 9 µm. For the planar texture, the cell is positioned under crossed polarizers, with the rubbing direction (R) at 45° to both the polarizer (P) and analyzer (A).

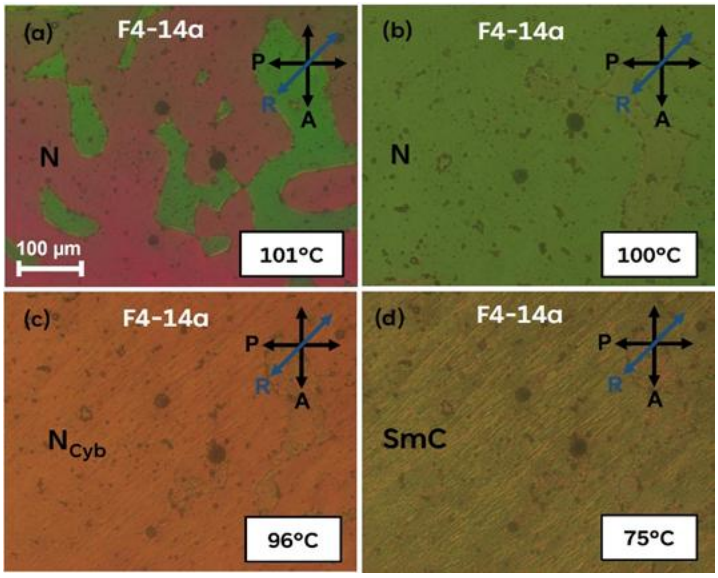

Fig. S19 POM micrographs of **F4-14a** at different temperatures in a planar cell (antiparallel buffing) of thickness 9 µm. The cell is kept under crossed polarizers with rubbing direction (R) at 45° with both the polarizer (P) and analyzer (A), respectively.

8. Dielectric Spectroscopy

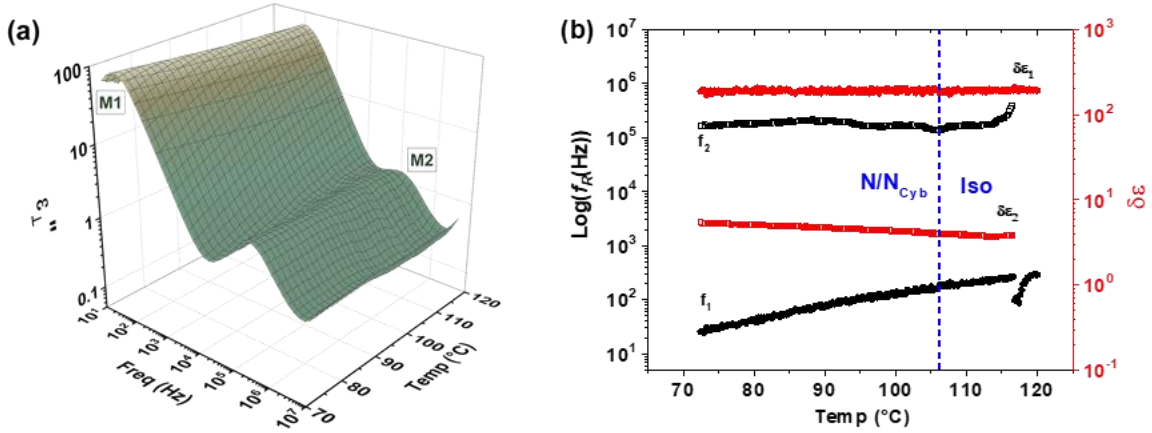

Fig. S20 (a) Dielectric loss spectra (ε'') of **F4-8a** as a function of temperature and frequency in a planar cell (b) Temperature variation of relaxation frequencies and corresponding dielectric strength of the LC based relaxation modes present in **F4-8a**.

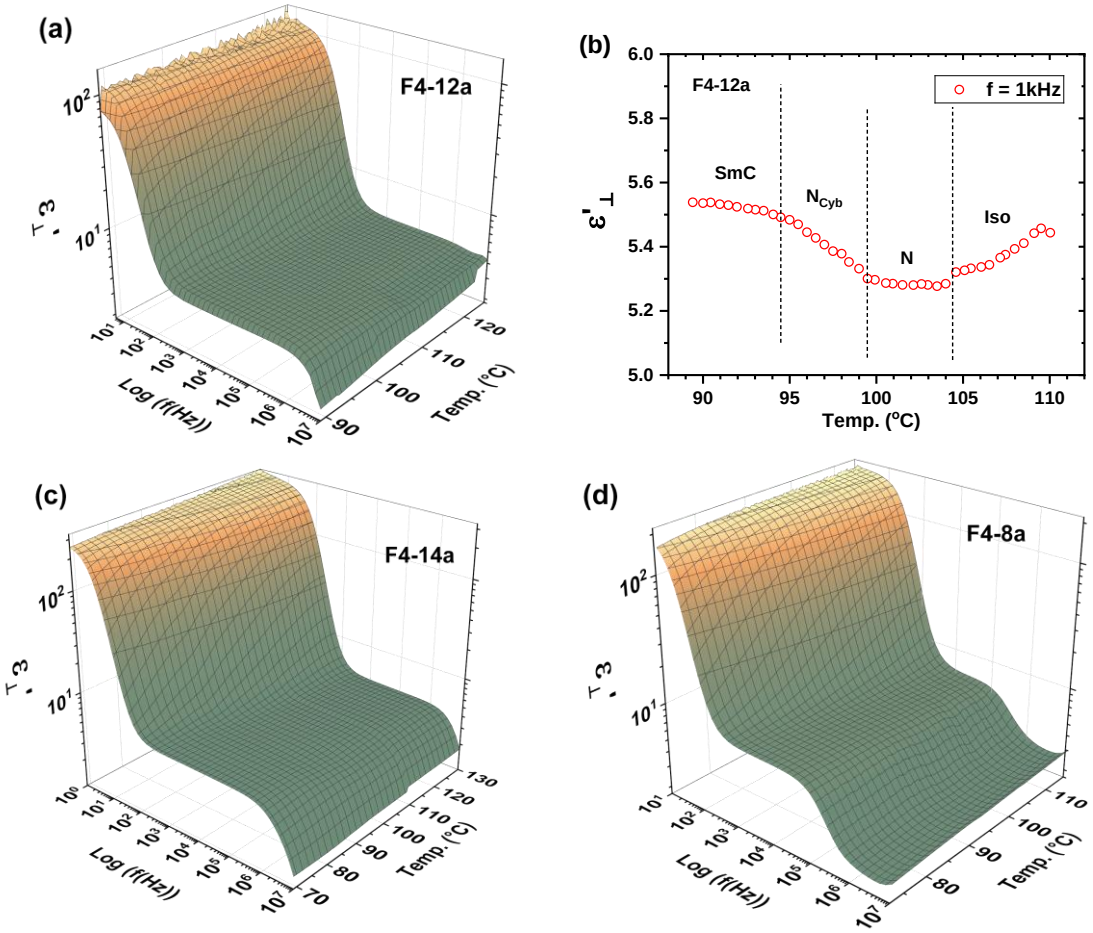

Fig. S21 Dielectric permittivity (ε') as a function of temperature and frequency for (a) **F4-12a**, (c) **F4-14a** and (d) **F4-8a** compounds filled in planar cells of 9µm thickness (b) The variation of ε' as a function of temperature at f = 1kHz for **F4-12a** molecule.

9. Spontaneous Polarization Studies

The spontaneous polarization (P_s) properties of the **F4-na** series of compounds were investigated using the field-induced repolarization current technique[3, 4] to assess the presence and nature of macroscopic polar ordering (ferroelectric properties). A triangular wave voltage (1 Hz-2 kHz, up to a large magnitude of 12 V_{pp} μm^{-1}) was applied across a 9 µm planar LC cell, and the electrical response was measured using a 1 kΩ or 10 kΩ test resistance. No measurable P_s was observed in the current responses obtained. **Fig. S22** and **S23** display the electrical response for **F4-14a** and **F4-8a**, respectively. The absence of measurable P_s is surprising, especially considering that dielectric spectroscopy results revealed the presence of cybotactic clustering, a collective relaxation process, and large ε' values in all three studied LC compounds (n = 8, 12, 14). Typically, cybotactic clusters in bent-core or U-shaped LC molecules form due to strong short-range polar ordering between molecules and are often considered a direct indicator of macroscopic polar ordering within the LC system.[5, 6] However, despite the presence of these clusters, no such polar ordering was detected in the electrical response of these compounds.

In the present case, despite the existence of clusters, there is no ferroelectric-like response in any of the LC phases of the studied homologues. This lack of response may occur if the LC molecules within the clusters are oriented anti-parallel to each other, resulting in a lower net dipole moment for the cybotactic clusters. Consequently, achieving macroscopic ferroelectric ordering becomes difficult, even with large cluster sizes. Similar findings for unsymmetrical bent-core molecules have been reported[7, 8] by Patranabish et al. and Nafees et al. Their studies demonstrated that increasing terminal chain lengths in these molecules suppresses polar ordering within the LC mesophases, as longer terminal chains tend to favor anti-parallel alignment to minimize steric effects. This behavior may explain the inability of our molecular samples to form ferroelectric LC mesophases.

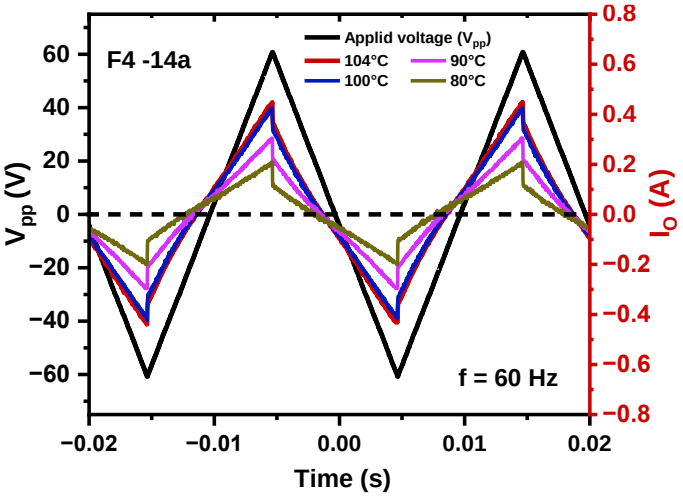

Fig. S22 Current response curve to a triangular wave input voltage for **F4-14a** in a planar cell of 9 µm thickness.

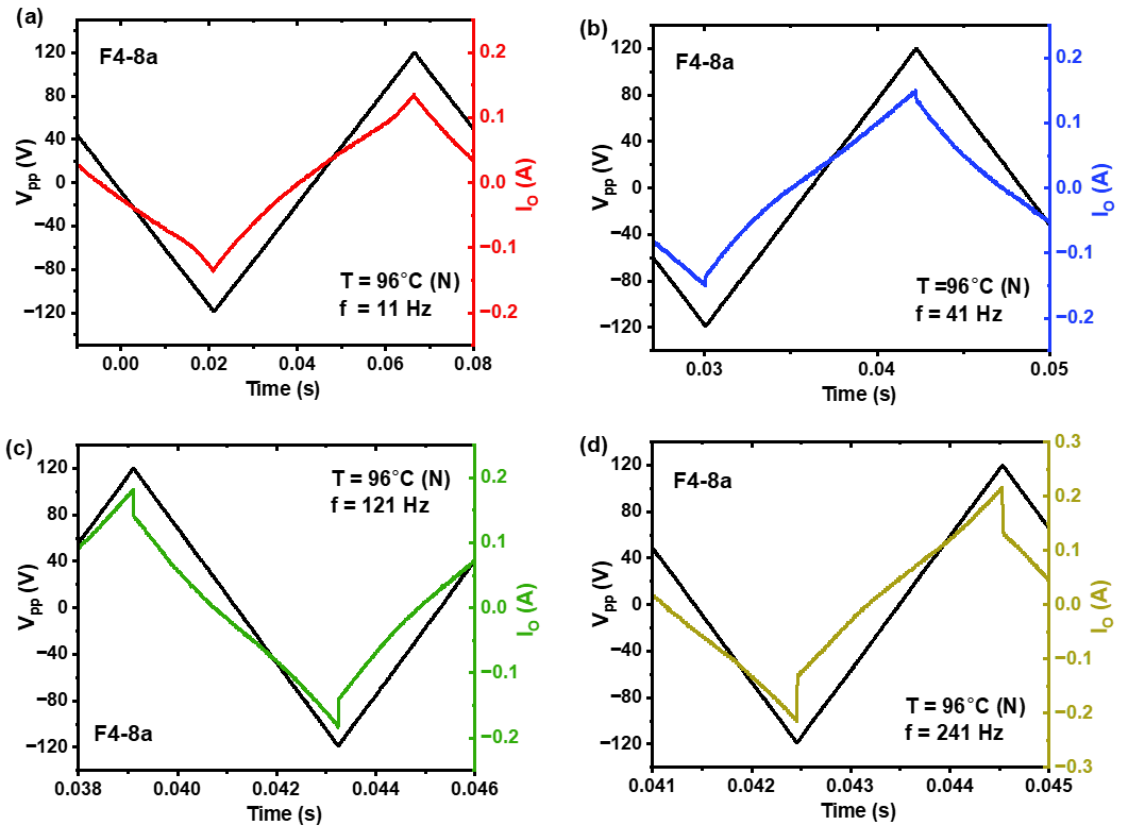

Fig. S23 Current response for a triangular input voltage for **F4-8a** in a planar cell of 9 µm thickness. In the N phase of **F4-8a**, a magnitude of input voltage (~12 V/µm) was applied across varied frequencies, but still no polarization peak was observed.

10. Electroconvection Studies

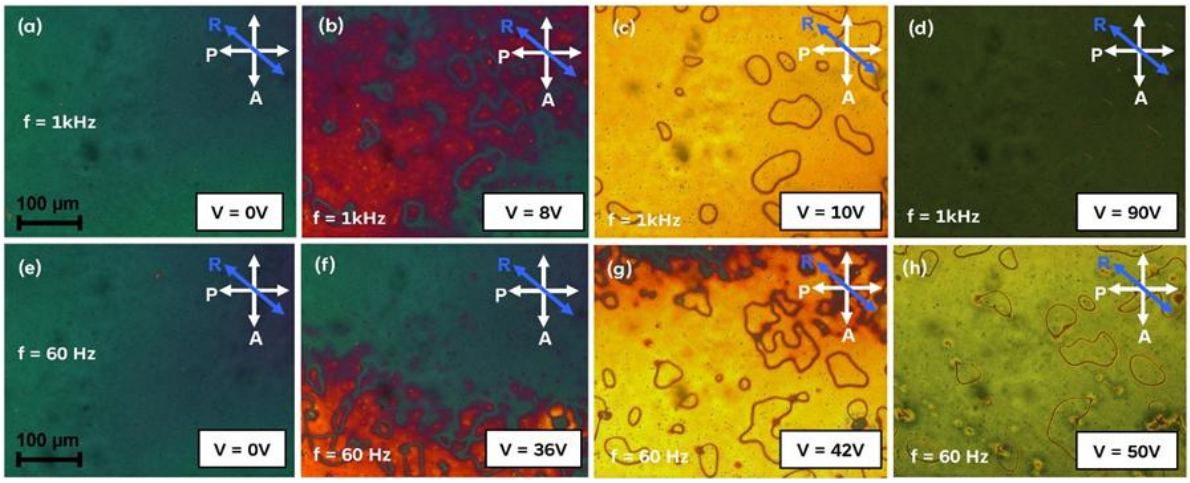

Fig. S24 Optical micrographs showing the response of **F4-12a** molecule in the N phase (T = 104 °C) under the action of applied AC voltage at two different frequencies, f = 1kHz **(a-d)** and f = 60Hz **(e-h)**. The POM textures are taken under crossed polarizers with rubbing direction (R) at 45° to either of the polarizer and analyzer. We have observed that under the action of external voltage at either of the frequencies, **F4-12a** exhibits a conventional FT which is facilitated by domain formations **(c,g)**.

In **F4-12a**, no EC patterns were observed. Instead, a more homogeneous and complete FT was noted. However, applying AC voltage at both frequencies led to the formation of two distinct domains (Fig. S24c and S24g), which eventually merged into a homeotropic state. A similar domain formation during the FT from planar to homeotropic was reported[2] by Kaur et al. in the N_{cyb} phase of unsymmetrical bent-core molecules. Interestingly, the behavior of **F4-8a** and **F4-12a** in the nematic phase shows significant differences. Since EC patterns are highly sensitive to LC anisotropies and cell configuration, a systematic study of EC patterns as a function of terminal alkoxy chain length and physical LC parameters in the **F4-na** series is essential. These findings suggest a scope for further investigation, which will be the subject of a separate manuscript.

11. Blue Phase Induction Through Doping

The **F4-na** series of compounds were doped with 5CB and S811 using their respective chloroform solutions, which were carefully measured to prepare various mixtures with different relative weight percent ratios, as outlined in **Table S6-S7**. These mixtures were then subjected to sonication for 30 min to ensure thorough mixing, followed by evaporation of the solvent. Subsequently, the samples were dried under vacuum conditions. The resulting mixtures were then transferred onto glass slides, and were observed under POM at slow cooling rates ranging from 1 to 5 °C min^{-1}. During cooling, the transition from the isotropic phase to the BP was observed, followed by further transformation into the N* (cholesteric) phase, and subsequent crystallization. The temperature ranges corresponding to the BP are provided in **Table S6-S7** for the respective mixtures, indicating the temperature range within which this phase transition occurs.

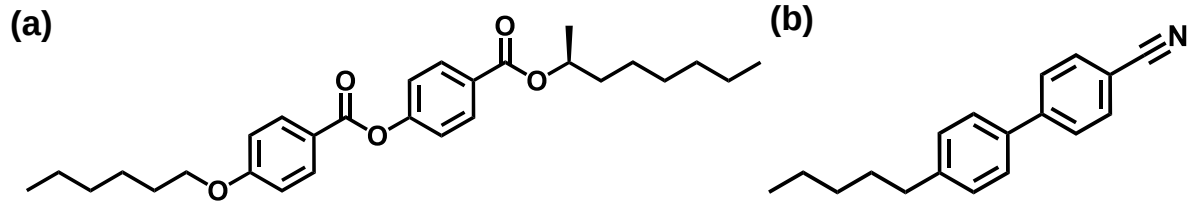

Fig. S25 Molecular structure of (a) Chiral dopant (**S811**) (S)-octan-2-yl 4-((4-(hexyloxy)benzoyl)oxy)benzoate (b) Room temperature LC (**5CB**) 4'-pentyl-[1,1'-biphenyl]-4-carbonitrile.

Table S6. Formation of BP observed in various mixtures (observed at cooling rate 5 °C min^{-1}), indicating initial and final temperatures recorded during cooling, along with the corresponding temperature range (presented within brackets []) in °C, where Iso: Isotropic, BP: Blue Phase. BP converts to the N* phase below the mentioned temperatures.

F4-na	BP temperature range for weight % composition F4-na:5CB:S811		
	35:45:20	25:45:30	45:25:30
n = 8	Iso 50.2 BP 43.9 [6.3]	Iso 29.9 BP 27.1 [2.8]	Iso 51.7 BP 43.9 [7.8]
n = 12	Iso 51.4 BP 43.3 [8.1]	Iso 29.2 BP 23.9 [5.3]	Iso 54.7 BP 50.4 [4.3]
n = 14	Iso 54.4 BP 52.3 [2.1]	Iso 36.2 BP 34.1 [2.1]	---
n = 16	Iso 47.5 BP 45.1 [2.4]	---	---
n = 18	---	---	---

Table S7. Formation of BP observed in various mixtures (observed at cooling rate 5 °C min^{-1}), indicating initial and final temperatures recorded during cooling, along with the corresponding temperature range in °C. BP converts to the N* phase below the mentioned temperatures.

Composition F4-8a:5CB:S811	Transition temperatures for BP (°C)	Total BP range (°C)
90:0:10	Iso 81.8 BP 70.8	11.0
80:0:20	Iso 51.9 BP 74.8	22.9
70:0:30	Iso 64.5 BP 48.0	16.5
60:0:40	Iso 46.1 BP 41.2	4.9
50:0:50	---	---
15:55:30	Iso 25.0 BP 19.2	5.8
20:50:30	Iso 28.6 BP 23.2	5.4
25:45:30	Iso 29.9 BP 27.1	2.8
30:40:30	Iso 36.9 BP 28.0	8.9
35:35:30	Iso 40.3 BP 35.9	4.4
40:30:30	Iso 46.7 BP 41.1	5.6
45:25:30	Iso 51.7 BP 43.9	7.8
50:20:30	Iso 49.5 BP 46.2	3.3
55:15:30	Iso 51.4 BP 48.5	2.9
15:40:45	---	---
20:40:40	---	---
25:40:35	---	---
30:40:30	Iso 36.9 BP 28.0	8.9
35:40:25	Iso 41.2 BP 33.8	7.4
40:40:20	Iso 48.3 BP 41.1	7.2
45:40:15	Iso 54.7 BP 51.3	3.4
50:40:10	Iso 69.9 BP 68.2	1.7
55:40:5	---	---

12. Density Functional Theory Calculations

Density functional theory (DFT) calculations on **F4-na** were performed using Gaussian 16 package and GaussView 5.0. Geometry optimizations were conducted employing the B3LYP exchange-correlation functional and a 6-31G (d,p) basis set, without imposing geometry constraints. These optimizations provided valuable insights[1] into the dipole moment, molecular conformation in space (bent architecture), as well as bond lengths and bond angles. Additionally, the HOMO-LUMO orbitals and electrostatic potential distribution over the molecular surface were visualized. A high HOMO-LUMO gap of ~ 4.16 eV signifies a higher energy threshold for electronic transitions. The HOMO/LUMO and ESP analyses provide insights into the overall electron density distribution of the bent-shaped molecule investigated in this work. They offer valuable information for understanding, probing, and potentially connecting the polarization behavior of bent-core molecules under an electric field. These further provide a deeper understanding of molecular polarity and its impact on phase behavior along with information about the kinetic stability of the system.[9] However, this aspect of the study is beyond the scope of the present manuscript. The relevant data is presented in **Fig. S26-S28** and **Table S8.**

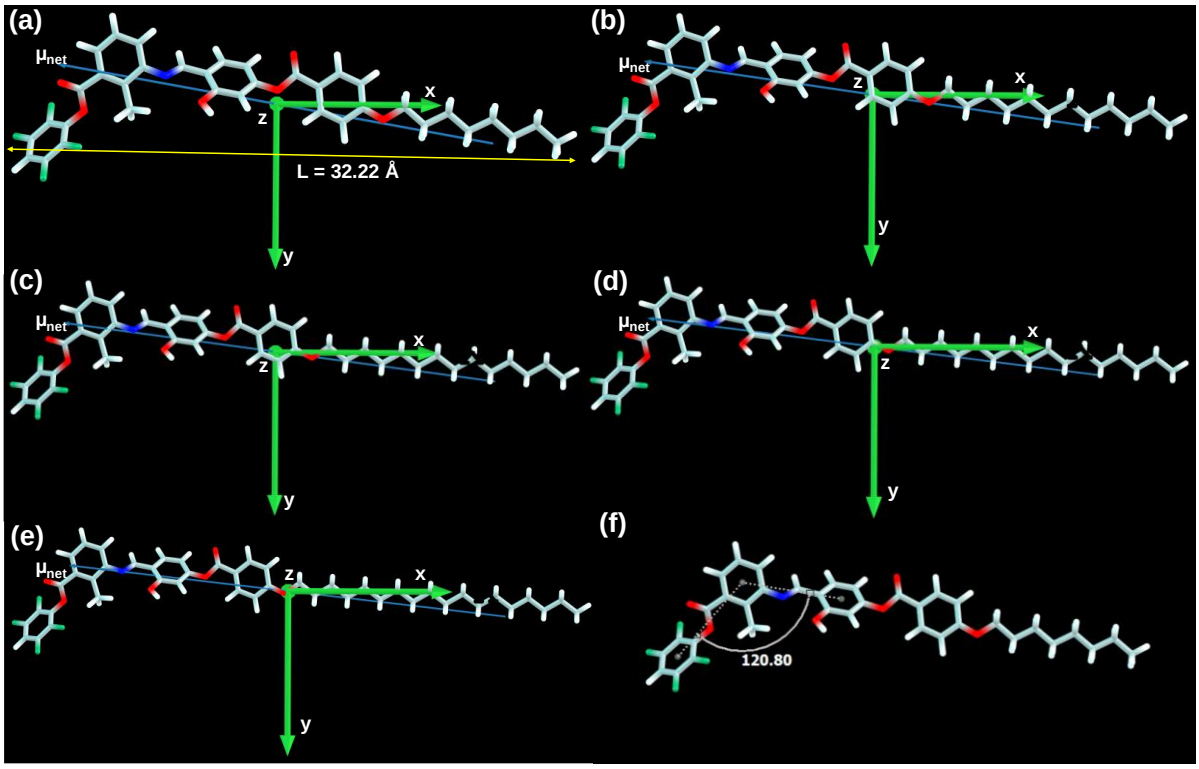

Fig. S26 DFT-optimized structures of **F4-na** bent-core compounds are presented, with the coordinate system shown in the figure indicating the x, y, and z axes. The blue arrow represents the net dipole moment direction (μ_{net}). (a)-(e) depict optimized structures for different homologues **F4-na** (n = 8, 12, 14, 16, and 18, respectively). The molecular length (L) is illustrated by the yellow line, calculated from the terminal fluorine (F) of the aromatic ring end to the terminal hydrogen (H) of the chain end. Further, (f) illustrates the bent angle in **F4-8a**, measured from the center of the molecular core to the centroid of the adjacent rings.

Table S8. Parameters calculated from DFT-optimized structures.

Compound	$\mu_{resultant} = (\mu_x^2 + \mu_y^2 + \mu_z^2)^{1/2}$ (Debye)	Bend-angle (°)	Molecular Length, L (Å)	HOMO (eV)	LUMO (eV)
F4-8a	9.32	120.8	32.22	-5.81	-1.65
F4-12a	9.36	120.7	37.30	-5.81	-1.65
F4-14a	9.37	120.8	39.88	-5.81	-1.65
F4-16a	9.38	120.8	42.44	-5.81	-1.65
F4-18a	9.38	120.8	45.00	-5.81	-1.65

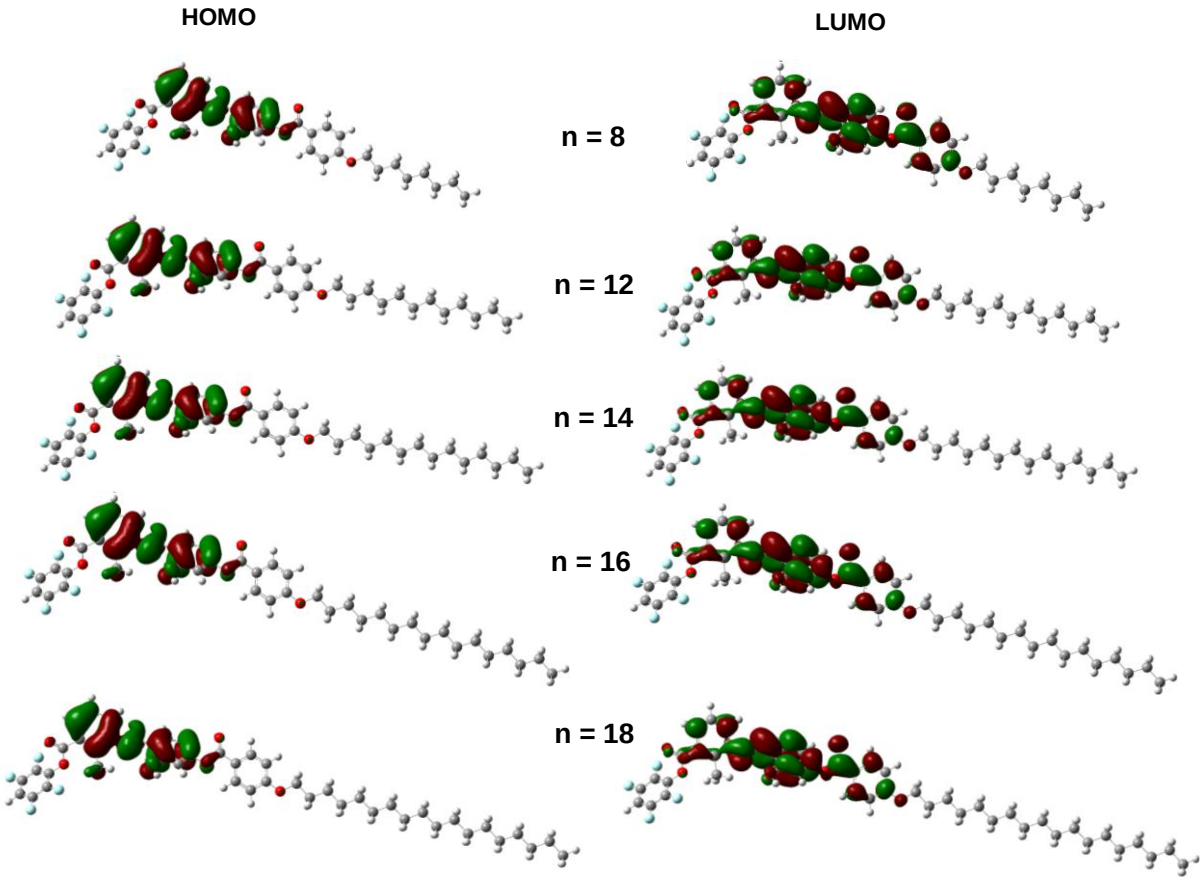

Fig S27 Optimized geometries of the **F4-na** series showing HOMO and LUMO molecular orbitals.

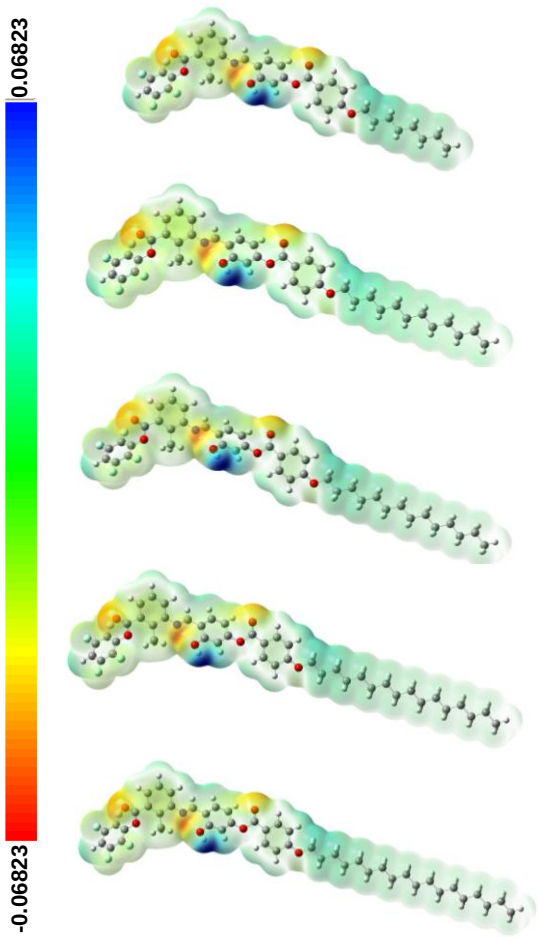

Fig. S28 Distribution of Electrostatic Potential (ESP) across the molecular surface, revealing polar regions influenced by the highly fluorinated terminal group and bent-core architecture.

13. References

1. A. Baghla, V. Punjani, D. S. Rao, S. K. Prasad and S. K. Pal, *J. Mater. Chem. C*, 2024, **12**, 3915-3923.
2. S. Kaur, G. Mohiuddin, J. Zhang, S. Chakraborty, X. Ding, D. Verma, A. Sinha, Y. Xiang and S. K. Pal, *J. Mol. Liq.*, 2023, **387**, 122626.
3. G. Shanker, M. Nagaraj, A. Kocot, J. K. Vij, M. Prehm and C. Tschierske, *Adv. Funct. Mater.*, 2012, **22**, 1671-1683.
4. G. Shanker, M. Prehm, M. Nagaraj, J. K. Vij, M. Weyland, A. Eremin and C. Tschierske, *ChemPhysChem*, 2014, **15**, 1323-1335.
5. S. Ghosh, N. Begum, S. Turlapati, S. K. Roy, A. K. Das and N. V. Rao, *J. Mater. Chem. C*, 2014, **2**, 425-431.
6. N. Sebastián, S. Belau, A. Eremin, M. Alaasar, M. Prehm and C. Tschierske, *Physical Chemistry Chemical Physics*, 2017, **19**, 5895-5905.
7. S. Patranabish, G. Mohiuddin, N. Begum, A. R. Laskar, S. K. Pal, N. V. Rao and A. Sinha, *J. Mol. Liq.*, 2018, **257**, 144-154.
8. A. Nafees, G. Kalita, M. K. Paul, A. Sinha and N. V. Rao, *RSC Adv.*, 2015, **5**, 7001-7006.
9. D. Bhattacharjee, T. K. Devi, R. Dabrowski and A. Bhattacharjee, *J. Mol. Liq.*, 2018, **272**, 239-252.